Evaluating Cumulus Parameterization Schemes for the Simulation of Arabian Peninsula Winter Rainfall

Raju Attada[1,2], Hari Prasad Dasari[1], Ravi Kumar Kunchala[3], Sabique Langodan[1], Niranjan Kumar Kondapalli[4], Omar Knio[5], and Ibrahim Hoteit[1,*]

1. Physical Sciences and Engineering Division, King Abdullah University of Science and Technology (KAUST), Thuwal, Saudi Arabia
2. Department of Earth and Environmental Sciences, Indian Institute of Science Education and Research, Mohali, India
3. Centre for Atmospheric Sciences, Indian Institute of Technology Delhi, New Delhi, India
4. Space and Atmospheric Sciences Division, Physical Research Laboratory, India
5. Computer, Electrical, and Mathematical Science and Engineering, King Abdullah University of Science and Technology (KAUST), Thuwal, Saudi Arabia

Revision Submitted to
Journal of Hydrometeorology

[*]**Corresponding author:** Prof. Ibrahim Hoteit
King Abdullah University of Science and Technology (KAUST)
Physical Science and Engineering Division
Thuwal 23955-6900, Saudi Arabia
E-mail: ibrahim.hoteit@kaust.edu.sa

Early Online Release: This preliminary version has been accepted for publication in *Journal of Hydrometeorology,* may be fully cited, and has been assigned DOI 10.1175/JHM-D-19-0114.1. The final typeset copyedited article will replace the EOR at the above DOI when it is published.

Abstract

This study investigates the sensitivity of winter seasonal rainfall over the Arabian Peninsula (AP) to different convective physical parameterization schemes using a high resolution WRF model. Three different parameterization schemes: Kain-Fritch (KF), Betts-Miller-Janjic (BMJ), and Grell-Freitas (GF) are used in winter simulations from 2001 to 2016. Results from seasonal simulations suggest that simulated AP winter rainfall with KF is in best agreement with observed rainfall in terms of spatial distribution and intensity. Higher spatial correlation coefficients and less biases with observations are also obtained with KF. In addition, the regional moisture transport, cloud distribution, and cloud microphysical responses are better simulated by KF. The AP low-level circulation, characterized by the Arabian Anticyclone, is well captured by KF and BMJ, but its position is displaced in GF. KF is further more successful at simulating the moisture distribution in the lower atmosphere and atmospheric water plumes in the middle troposphere. The higher skill of rainfall simulation with the KF (and to some extent BMJ) is attributed to a better representation of the Arabian Anticyclone and subtropical westerly jet, which guides the upper tropospheric synoptic transients and moisture. In addition, the vertical profile of diabatic heating from KF is in better agreement with the observations. Discrepancies in representing the diabatic heating profile by BMJ and GF show discrepancies in instability and in turn precipitation biases. Our results indicate that the selection of sub-grid convective parameterization in a high-resolution atmospheric model over the AP is an important factor for accurate regional rainfall simulations.

Keywords: Arabian Peninsula, Rainfall, WRF model, Convective parametrizations, Sensitivity analysis.

Accepted for publication in *Journal of Hydrometeorology*. DOI 10.1175/JHM-D-19-0114.1.

1. Introduction

The Arabian Peninsula (AP) is one of the driest and most water-limited environments in the world, where the availability of fresh water is of major regional concern (Osman-Elasha, 2010; Barlow et al., 2015). There are no rivers with perennial stream flow, and water supplies in the Kingdom of Saudi Arabia are principally derived from rainfall, mined groundwater, and (more recently) desalination (Ouda, 2013). Rapid socio-economic development, expansion of urbanization, agricultural activities, and high population growth are intensifying the stress on water supplies in the region. The reported increase in drought episodes (Ragab and Prudhomme, 2000; Kumar et al., 2017) along with the anticipated warmer future climate (Almazroui et al., 2016a; Attada et al., 2018; 2019a,b) will further stress the management of water resources. It is thus essential to understand in detail the spatio-temporal variability of rainfall over the AP, to enable its accurate prediction and design efficient strategies for mitigating water scarcity and associated risks.

The availability of accurate datasets is key to studying regional rainfall variability; however, observations and associated rainfall information over the AP are lacking. Global reanalysis datasets are a crucial source of information for regions with limited observed data records. However, global climate reanalyses are still coarse, with resolutions on the order of 50–100 km, not sufficient for investigating regions with complex topography, such as the western and eastern AP (Almazroui, 2015; Zittis and Hadjinicolaou, 2017). In such areas, regional climate models with finer grid spacing are more appropriate to resolve the local-to-regional processes that interact with the large-scale circulations (e.g. Gao et al., 2017). Validated high-resolution simulations may provide the relevant information at sufficient spatial and temporal scales for data sparse regions to enable studying and predicting regional rainfall variability.

Most (75%) of the AP annual rainfall falls in winter, from November through April, which

Accepted for publication in *Journal of Hydrometeorology*. DOI 10.1175/JHM-D-19-0114.1.

is known as the wet season for the region (Almazroui, 2011; Dasari et al., 2018). Convective rainfall predominates with high spatial variability over the region, as a result of the strong impact of complex terrain on the initiation and organization of convective processes (Kumar et al., 2015; and references therein). High resolution modelling with a suitable cumulus parameterization could be used to provide a reliable characterization of regional convection processes. In this respect, Prein et al. (2015) presented a detailed review of the different aspects of high-resolution convection modelling and concluded that the choice of cumulus parametrization scheme (CPS) is an important factor in the simulation of convective precipitation. Cumulus convection has a major effect on the hydrological cycle through the release of latent heat, on the vertical transport of sensible heat, water vapor, and momentum (Han et al., 2016). It is therefore necessary to develop models that accurately represent the interactions between cumulus convection and these movements within a large-scale environment in order to obtain viable weather and climate simulations and subsequent predictions.

Identifying the most suitable CPS for a particular region is crucial for reliable simulation of rainfall. Among the many available CPS schemes, extensive tests have been conducted on the Grell scheme (Grell et al., 1993; Grell and Devenyi, 2002), which was originally based on Arakawa and Schubert (1974); the BMJ scheme (Betts and Miller, 1986; Janjic, 1994); and the KF scheme (Kain and Fritsch, 1993; Kain, 2004), which was developed based on Fritsch and Chappell (1980). Various sensitivity studies with respect to the CPS have also focused on reproducing climatological rainfall. For instance, Giorgi and Shields (1999) suggested that the Grell Scheme produces a realistic regional climate over the continental United States, although Liang et al. (2004) later reported the superiority of the KF for simulating North American regional climate rainfall.

Accepted for publication in *Journal of Hydrometeorology*. DOI 10.1175/JHM-D-19-0114.1.

Almazroui (2016a;b) recently used a 50-km regional climate model (RegCM) to investigate the impact of different CPSs in the Middle East and North Africa (MENA) over a limited time period of 5 years. The study reported that rainfall over the AP is quite sensitive to the cumulus parameterization. Similar studies have also been conducted again over short time-frames and using relatively coarse resolution models (e.g. Evans et al., 2004; Almazroui 2016a). The complex AP terrain may induce low-level convergence and upslope winds through valleys. This may significantly impact the stimulation and growth of deep convection (Bennett et al., 2011; Wang et al., 2016) and cannot be resolved with coarse resolution models. The sensitivity of convective precipitation over the complex terrain on the AP with respect to different CPSs has yet to be studied using a high resolution model.

Several studies have investigated the sensitivity of rainfall simulations to CPSs in various regions. For instance, some studies highlighted the importance of choosing a suitable combination of parameterization schemes within the Weather Research and Forecasting (WRF) model to simulate the rainfall features over the Indian region (Mukhopadhyay et al., 2010; Srinivas et al., 2013; Ratnam et al., 2017). Similar efforts have been conducted for Australia (Evans et al., 2012, Kala et al., 2015), Spain (Argueso et al., 2011), Europe (Mooney et al., 2013), China (Yuan et al., 2012), South Africa (Crétat et al., 2012, Ratna et al., 2014), and the MENA region (e.g. Zittis et al., 2014; Ehsan et al. 2017).

This study investigates the sensitivity of WRF simulated rainfall at seasonal scales over the AP with respect to the choice of CPSs based on a high-resolution (5 km) configuration capable of resolving the complex regional topography during the period 2001 to 2016. The selected CPSs are analyzed in terms of their ability to effectively simulate the magnitude and spatial patterns of rainfall and associated physical processes, and are further tuned to enhance the precipitation

Accepted for publication in *Journal of Hydrometeorology*. DOI 10.1175/JHM-D-19-0114.1.

simulations. The remainder of the paper is organized as follows. Section 2 describes the data and methodology, which also outlines the model configurations and the design of the numerical experiments. Sections 3 and 4 present and analyze the results. A summary of the main conclusions is offered in Section 5.

2. Model, Data, and Methods

2.1 Model details and experimental configuration

We implemented a non-hydrostatic Advanced Research WRF model (Version 3.8.1; Skamarock et al., 2008) with terrain following coordinates and a constant pressure surface at the top. The model configuration includes two two-way nested domains with respective horizontal resolutions of 15 km and 5 km, each with 52 vertical sigma levels. The chosen model domain extends between 30°W to 130°E in the zonal direction and 30°S to 45°N in the meridional direction is used to resolve the large-scale atmospheric features and internal dynamics of the system (e.g. Wang et al., 2004; Lucas-Picher et al., 2011; Raju et al., 2015a, b). The initial and 6-hourly boundary conditions are taken from the European Centre for Medium-Range Weather Forecasts Interim Reanalysis (ERAI) data available at a resolution of 0.75°. Sea surface temperature (SST) data are also prescribed from the ERAI dataset. For each winter season, simulations are conducted from November 1 to April 1, with the first month used as a spin-up period to remove spurious effects.

The sensitivity of the model to the following three CPSs is investigated: Kain-Fritsch (KF) (Kain and Fritsch, 1993; Kain, 2004), Betts-Miller-Janjic (BMJ) (Betts and Miller, 1986; Janjic, 1994), and the scale-aware Grell-Freitas (GF) (Grell and Freitas, 2014):

(i) KF is a simple mass-flux cloud model for moist updraft/downdraft. It includes a trigger function to initiate convection, compensating for circulation, and closure assumption.

Accepted for publication in *Journal of Hydrometeorology*. DOI 10.1175/JHM-D-19-0114.1.

(ii) BMJ is a convective-adjustment-type scheme that was developed to adjust atmospheric instabilities (toward a reference profile derived from a climatology) by triggering deep convection, when sufficient moisture is available.

(iii) GF is an ensemble scheme, in which multiple cumulus schemes and variants are run within boxes to obtain an ensemble-mean realization. The ensemble members use different parameters for updraft/downdrafts entrainment/detrainment. It is an updated Grell-Dévényi scheme (Grell and Devenyi, 2002), such that the scale awareness is improved by introducing the method of Arakawa et al. (2011). This relaxes the assumptions of traditional parameterizations in which convection is contained within individual model grid columns when the fractional area covered by convection clouds is small.

All other physical parameterizations are the same in all experiments and are as follows: the Thompson (Thompson et al., 2016) microphysical scheme (Hong and Lim, 2006) for cloud processes, the Rapid Radiative Transfer Model for Global circulation models (RRTMG) for both longwave and shortwave radiation (Iacono et al., 2008) processes, and the Mellor-Yamada-Nakanishi-Niino turbulent kinetic energy scheme (Nakanishi Niino, 2004) for the planetary boundary layer. Land surface processes are resolved using the Noah land surface model scheme (Chen and Dudhia, 2001) with four soil layers. Three sets of experiments were conducted for each season during the period 2001 to 2016. The 5 km (inner domain) simulations were analyzed to identify the differences between the model simulations that are solely attributed to the different CPSs.

2.2 Data and Methods

Accepted for publication in *Journal of Hydrometeorology*. DOI 10.1175/JHM-D-19-0114.1.

Daily precipitation data with a spatial grid resolution of 0.25° × 0.25° were obtained from the Tropical Rainfall Measuring Mission (TRMM) version 7 (hereafter referred to TRMM; Huffman et al., 2007, 2010). This product combines precipitation estimates from various satellite systems (both infrared and radar) and a surface-gauge analysis on a grid at 3-hourly intervals. Almazroui (2011) compared the TRMM gridded rainfall data with rain gauge observations over the AP and concluded that the TRMM rainfall data is in good agreement with the observations, which was lately confirmed by Hasanean and Almazroui, (2015) and Sultana and Nasrollahi (2018). We also evaluated the model-simulated temperature, specific humidity, geopotential height and horizontal wind vectors at different pressure levels against the National Aeronautics and Space Administration's Modern-Era Retrospective Analysis for Research and Applications Version 2 (MERRA-2, Gelaro et al., 2017), which is available on an 0.58° × 0.625°grid. Mean monthly cloud information from the Clouds and the Earth's Radiant Energy System (CERES) database available at a spatial resolution of 1°×1° was also used to assess the model-simulated cloud characteristics.

To quantitatively assess the model simulations, statistical scores such as mean bias, Root Mean Square Error (RMSE), Standard Deviation (SD), and the spatial pattern correlation coefficient (PCC) were computed. Tables 1 and 2 present the four statistical metrics of rainfall and temperature for the entire AP and for three different sub-regions: the southern AP (SAP; 12– 22° N, 35–60° E), the northern AP (NAP; 22–32° N, 35–60° E), and the northeastern AP (NEAP; 22–35° N, 45–60° E). The selection of these sub-regions was based on their regional climate characteristics, as suggested by previous studies (e.g. Almazroui, 2012; Athar et al., 2014; Kang et al., 2015; Attada et al., 2019a). A two-tailed significance test was performed using a Student's t-distribution to evaluate the statistical significance of the results. The vertically integrated moisture transport (kg m^{-1} s^{-1}) was estimated as,

Accepted for publication in *Journal of Hydrometeorology*. DOI 10.1175/JHM-D-19-0114.1.

$$VIMT = \frac{1}{g}\int_{P_t}^{P_s} qV dp,$$

where V is the horizontal velocity, q is specific humidity, P_s is surface pressure, P_t is the pressure at the top of the air column, and dp is the vertical incremental change in pressure.

We further computed and analyzed the apparent heat source (e.g. Yanai et al., 1973) to determine the thermodynamical feedbacks to the seasonal mean precipitation and to identify the convective parameterization deficiencies in the model. The apparent heat source (Diabatic heating) is computed as the sum of the latent heating associated with phase changes, the vertical transport, the sub-grid diffusion, and the radiative heating (e.g. Liu and Moncrieff, 2007).

$$\text{Apparent heat source} = C_p \left(\frac{p}{p_0}\right)^k \left(\frac{\partial\theta}{\partial t} + V \cdot \nabla\theta + \omega \frac{\partial\theta}{\partial p}\right),$$

where θ is the potential temperature, V is the horizontal velocity, ω is the vertical velocity, and p is the pressure. k = R/Cp, where R and Cp are, respectively, the gas constant and the specific heat at constant pressure of dry air; p_o = 1000 hPa.

3. Results and discussion

We first evaluate the sensitivity of the model simulated rainfall to different CPSs with respect to the TRMM observations. We then analyze the circulation, temperature, moisture and cloud distributions to understand the dynamic and thermodynamic responses of the model rainfall to the selected convective schemes.

3.1 Evaluation of seasonal rainfall

Fig. 1 shows a comparison of the spatial distribution of winter (DJFM) TRMM observed total seasonal rainfall with WRF simulations with the different CPSs, KF, BMJ, and GF over the period

Accepted for publication in *Journal of Hydrometeorology*. DOI 10.1175/JHM-D-19-0114.1.

2001-2016. High rainfall bands are located over the NAP, the Arabian Gulf, and the Mediterranean region. A considerable amount of rainfall is also observed in the narrow zones over the southwestern AP followed by the central and southern parts of the Sarawat mountain ranges (Fig. 1a). The high rainfall in the NAP is mainly related to the passage of Mediterranean cyclonic storms (midlatitude westerlies). The alignment of the mountains along the coast of the Mediterranean Sea also influences the precipitation distribution in the NAP by creating a pronounced lee effect with rapidly decreasing rainfall toward the northeast. It is also noticeable that precipitation decreases from north to south, with a minimal (or no) rain, observed over the SAP (referred to as a dry zone), particularly over the Rub Al-Khali (the world's largest desert) region.

These observed rainfall features are simulated reasonably well with KF (Fig. 1b) and BMJ (Fig. 1c). However, GF (Fig. 1d) simulates an extremely dry area over the entire region of Saudi Arabia, except the eastern Mediterranean and the southern Red Sea. Although BMJ and KF underestimate the rainfall compared to observations over the Northeastern AP, KF produces spatial patterns of rainfall that are more realistic than those of BMJ and GF. KF also interestingly produces major precipitation zones over the AP: one located in NEAP and the other over the south-central Red Sea (with 80–150 mm), which is known as the Red Sea Convergence Zone (RSCZ). Northerly and southerly winds converge in this region and enhance convection, (e.g. de Vries et al., 2013; Viswanadhapalli et al., 2016; Dasari et al., 2018), and this effect is more realistically resolved by KF and BMJ compared to the observed rainfall. The spatial correlation coefficients between the observed rainfall and model simulations (KF, BMJ, and GF) suggest that the superiority of KF, with a higher correlation coefficient 0.71 compared to 0.66 for BMJ and 0.19 for GF.

To achieve good fidelity of the WRF model with different CPSs, the model should not only capture the mean fields, but also generate variances that are consistent with those of the

Accepted for publication in *Journal of Hydrometeorology*. DOI 10.1175/JHM-D-19-0114.1.

observations. We therefore compared the standard deviations (SD) of rainfall as they result from the model with KF, BMJ, GF, and TRMM observations (Fig. 1e-h). TRMM (Fig. 1e) shows the highest (> 2 mm) SD over the NEAP and eastern Mediterranean regions. This seasonal mean rainfall variability is reproduced best with KF (Fig. 1f) and BMJ (Fig. 1g). The highest rainfall variability occurs over the NEAP compared to the other sub-regions, as reported in earlier studies (Kang et al., 2015; Abid et al., 2016). The weaker SD in GF is similar to the seasonal average, which has a lower magnitude (Fig 1d). KF and BMJ reproduce better the details of the rainfall variability in the southern Red Sea where RSCZ-induced rainfall is predominant. Overall, KF exhibits a spatial variability pattern and amplitude that is more in agreement with TRMM than the other two CPSs.

The biases between the observed and simulated rainfall are shown in Figs. 1j, 1k, and ll for KF, BMJ, and GF, respectively. All three schemes produce negative biases over the NEAP and positive biases over the SAP. KF shows a dry bias of approximately 0.8 to 1 mm day^{-1}, whereas BMJ and GF exhibit significant dry biases of around 1.5 to 1.8 mm day^{-1} and more than 2 mm day^{-1}, respectively. These dry biases are reflected in the higher RMSEs for all schemes and are more pronounced over the NEAP for BMJ and GF. The regional averaged RMSEs of rainfall over the AP are 0.29, 0.31, and 0.37 for KF, BMJ, and GF, respectively (Table 1). Overall, the analyses of mean rainfall patterns, SDs, and biases indicate that the model-simulated precipitation sensitive to the CPSs over the AP, with the KF outperforming the other two CPSs.

3.2 Seasonal evolution of rainfall

The time series of daily rainfall climatology from TRMM rainfall over the AP, NAP, and SAP are presented in Fig. 2 for each CPS. Based on the TRMM observations, the amount of precipitation and rainfall episodes are relatively highest in NAP (Figs. 2a,b,c). All CPSs simulated these

Accepted for publication in *Journal of Hydrometeorology*. DOI 10.1175/JHM-D-19-0114.1.

variations in the seasonal evolution of rainfall, but with lower magnitudes than in the observations. The seasonal variability of rainfall from GF is significantly dampened compared to BMJ and KF, which well reproduce the seasonal cycle as observed in TRMM for AP, NAP and SAP sub-regions. TRMM also suggests that the largest rainfalls occur during December and March over the AP and NAP, whereas over SAP the high rainfall is recorded during February and early March. With the exception of a few episodes, the simulated rainfall with KF, BMJ, and GF clearly exhibits a significant dry bias, throughout the winter season over the AP and NAP, and a wet bias over the SAP. All three CPSs depict the north-south rainfall gradients, with higher rainfall over NAP and lower over SAP, in agreement with the TRMM observations. The excess amount of rainfall over the NAP is attributed to the passage of midlatitude synoptic storms during winter (Almazroui et al., 2013; Barlow et al., 2015). Out of the three CPSs, the KF-simulated rainfall seasonal cycle closely follows the TRMM rainfall patterns, with daily peaks over the AP and its sub-regions.

In order to validate the model skill in simulating rainfall, different verification scores namely the equitable threat score (ETS), bias score (BS) and false alarm rate (FAR) are computed over a wide range of rainfall thresholds based on the contingency table suggested by Bhomia et al. (2019). Figure 3 shows the ETS, BS and FAR verification score at different rainfall thresholds varying from 1 to 15 mm over NAP. ETS first increases and then decreases for the higher rainfall thresholds of KF and BMJ. For KF, ETS has higher values at all rainfall thresholds compared to BMJ and GF. Note that KF and BMJ show lower skills for higher rainfall thresholds (above 12mm) whereas GF has the poorest performance. A gradual increase of BS is seen with increased rainfall thresholds. KF shows higher BS compared to BMJ for all the thresholds. FAR is increased rapidly with increased rainfall thresholds, and all CPSs has no/minimal skill for high thresholds. KF has low FAR values compared to BMJ and GF. Overall, the KF has a better rainfall skill compared to

Accepted for publication in *Journal of Hydrometeorology*. DOI 10.1175/JHM-D-19-0114.1.

the others two CPSs. The impact parameter (Wilks, 2006; Raju et al., 2018; Kumar et al., 2019) is also estimated to quantify the improvement/degradation of KF in simulating rainfall over GF and BMJ. The analysis (not shown) confirms that the KF has a better skill in simulating rainfall.

3.3 Assessment of spatial distribution of near surface temperatures

The presence of complex mountains to the west of AP is generally difficult to handle with numerical models, and may result in temperature bias which ultimately impacts the simulation of precipitation. The accurate representation of steep land-sea thermal gradients is one of the basic requirements for a model to simulate realistic rainfall distributions. To assess the simulated near surface temperature distributions in the model, we plot the mean seasonal winter daily mean temperature (2mT), maximum temperature (Tmax), and minimum temperature (Tmin) are plotted in Fig. 4 at 2 m height for the period 2001–2016 from MERRA-2 and the model with the three different CPSs. The mean 2mT from MERRA-2 (Fig. 4a) indicates low temperatures (< 288 K) over the NAP, moderate temperatures (288–296 K) over central and western AP, and higher temperatures (> 296 K) over SAP and the southern Red Sea (including Sudan and northern Ethiopian regions). KF (Fig. 3b) and BMJ (Fig. 4c) schemes simulate well the high temperature observed over the Rub Al-Khali desert region, and the north-south temperature gradients over the AP and the Red Sea (high temperatures over the southern Red Sea and low temperatures over the northern Red Sea). GF (Fig. 4d) underestimates the near surface 2mT patterns compared to MERRA-2. The temperatures in the southeastern AP are higher than in the southwestern AP, due to the local topography. The lowest temperatures (< 275 K) are confined to the NEAP region in all CPSs, and these are in good agreement with MERRA-2. All three CPSs simulate the lowest temperatures over the mountainous region, suggesting the effectiveness of a high-resolution WRF model in reproducing the lowest temperatures, namely by resolving local topography and their

Accepted for publication in *Journal of Hydrometeorology*. DOI 10.1175/JHM-D-19-0114.1.

effects on temperatures (e.g., Viswanadhapalli et al., 2016). The comparative statistics between MERRA-2 and the model-simulated 2mT, Tmax, and Tmin for the entire AP and sub-regions are outlined in Table 2. The spatial correlations between MERRA-2 and WRF with KF, BMJ, and GF are 0.96, 0.96, and 0.93, respectively. Over the NAP (SAP), these correlations are 0.96 (0.92), 0.95 (0.93), and 0.93 (0.91) with KF, BMJ, and GF, respectively; and for the NEAP, the three schemes provide even higher correlation coefficients of 0.97, 0.96, and 0.95, with KF being relatively higher than BMJ and GF.

To quantify the ability of WRF to describe mean temperatures, we further conducted different statistical skill score analyses over the AP and its sub-regions and these skill scores are statistically significant at 95% confidence level with the student-t test. The observations exhibit the highest variability over the NEAP, NAP, AP, and SAP with the values of 2.74 K, 2.59 K, 2.12 K, and 1.68 K, respectively. All three schemes produce higher temperature variability over the AP; with KF (2.97 K) performing relatively better than BMJ (3.07 K) and GF (3.30 K). Similar results were also obtained in other sub-regions of the AP (Table 2). BMJ and GF exhibit strong cold biases of approximately 2.1 K and 3.1 K over the AP, whereas the mean bias of KF is around 1.4 K, indicating the superiority of KF in simulating mean temperature patterns.

The salient characteristics of winter mean daily Tmax, such as the significant north–south gradient (higher temperatures over the SAP than the NAP) superimposed with coastal effects and localized orographic features observed in MERRA-2 (Fig. 4e), are well simulated by all CPSs, despite being slightly underestimated. MERRA-2 shows that the highest Tmax (> 300 K) occurs over Sudan and the SAP. KF (Fig. 4f), BMJ (Fig. 4g), and GF (Fig. 4h) show low Tmax over the NEAP and high Tmax over the SAP, including the Rub Al-Khali region as in MERRA-2. Relatively, lower Tmax values are noticeable over the eastern side of the Red Sea, suggesting the

Accepted for publication in *Journal of Hydrometeorology*. DOI 10.1175/JHM-D-19-0114.1.

influence of topography on the maximum temperature distribution in the WRF model. Overall, all CPSs underestimate the Tmax patterns over the AP, although they are able to simulate the north-south Tmax gradient. In terms of spatial distribution, KF simulates a realistic distribution of Tmax similar to that of MERRA-2; however, those of BMJ and GF are not as accurate, with GF significantly underestimating Tmax. Moreover, only KF successfully simulates the three distinct climate regimes (Attada et al., 2019a, b) over the AP that are observed in MERRA-2. In general, this meridional temperature gradient is mainly modulated by western disturbances originating in the Mediterranean region during winter (Viswanadhapalli et al., 2016; Dasari et al., 2018; Attada et al., 2019b). The pattern correlations between the model simulations and MERRA-2 over the AP reveal higher values for KF (0.91) than BMJ (0.89) and GF (0.84). Higher pattern correlations are also obtained for NEAP: 0.94, 0.94, and 0.92 using KF, BMJ, and GF, respectively. The SDs of Tmax are similar in magnitude to those of mean temperatures (Table 2), and Tmax has stronger negative biases compared to mean 2mT, with values of approximately -2.8 K, -3.5 K, and -4.1 K over the entire AP for KF, BMJ, and GF, respectively. For the mean temperature, GF leads to higher RMSEs than KF and BMJ over the AP and its sub-regions.

The comparison of simulated daily minimum temperatures (Tmin) with MERRA-2 (Fig. 4i-4l) suggests reasonable agreement for the north–south gradient over the AP and the high minimum over the Red Sea, southeastern AP, and the Arabian Gulf. The simulations also produce lower temperatures over Ethiopia and western Yemen, consistent with those of Almazroui (2012) using the RegCM model. The CPSs leads to significant differences when simulating minimum temperatures over the AP. Although all schemes underestimate minimum temperatures compared to MERRA-2, KF performs better, in terms of the regional distribution of temperatures, than BMJ and GF. The spatial distribution of the mean bias of Tmin (not shown) shows a strong cold bias

Accepted for publication in *Journal of Hydrometeorology*. DOI 10.1175/JHM-D-19-0114.1.

over the entire AP, in agreement with the findings of Viswanadhapalli et al. (2016). Furthermore, higher correlations with MEERA are obtained with KF simulated Tmin patterns over the AP and its sub-regions (Table 2). The SD of Tmin suggests that all CPSs exhibit a higher SD over NEAP than the other sub-regions, but are lower compared to MERRA-2. KF has less RMSE over the AP (1.4 K), NAP (1.2 K), SAP (1.6 K), and NEAP (1.5 K) compared to BMJ and GF (Table 2).

3.4 Seasonal cycle of daily mean, maximum, and minimum temperatures

Fig. 5 depicts the seasonal cycles of daily mean temperature, Tmax, and Tmin over the AP, NAP, and SAP over the period 2001–2016. The seasonal cycle of daily temperatures from MERRA-2 over the AP (Fig. 5a), NAP (Fig. 5b), and SAP (Fig. 5c) indicates peak temperatures during the last week of February. This seasonal evolution of temperatures is well re-produced by WRF using all CPSs. Overall, the temperature evolutions are similar in all climatic zones and are well captured (with some deviations) compared to MERRA-2. Over the AP and SAP, KF is better at producing mean temperatures, while GF is slightly better over the NAP. All CPSs simulate the peak temperatures earlier than MERRA-2.

The seasonal cycle of Tmax (Fig. 5d–5f) is similar to that of mean temperature, but varies between 292 K to 302 K. All three schemes capture the evolution of Tmax over the AP with notable underestimation compared to MERRA-2. KF performs better over the AP than over NAP and SAP, for which it produces cold biases. In the case of NAP, GF shows the best phase of Tmax evolution, while KF and BMJ depict colder biases. KF seems to not perform as well as BMJ and GF in simulating the maximum temperature evolution. In MERRA-2, the seasonal evolution of Tmin (Fig. 5h–5i) varies between 284 K and 286 K over the AP; 281 K to 283 K over the NAP; and 289 K to 294 K over the SAP. All three schemes simulate these evolutions of Tmin over the AP sub-

Accepted for publication in *Journal of Hydrometeorology*. DOI 10.1175/JHM-D-19-0114.1.

regions with considerable discrepancies. They also underestimate the seasonal cycle compared to MERRA-2, with KF performing relatively better than BMJ and GF.

3.5 Monthly variations in rainfall and temperature biases

The sub-regional average precipitation and temperature biases computed for the individual months of December, January, February, and March between the model simulations with different CPSs and TRMM observations are presented in Fig. 6. Monthly variations in the rainfall biases of KF are smaller than those of BMJ and GF for all regions. Over the AP, the rainfall bias ranges between -0.1 and 0.21 mm day^{-1} with KF, between -0.1 to 0.30 mm d^{-1} with BMJ, between -0.19 to 0.35 mm d^{-1} with GF. All CPSs simulate the wet bias in the month of February and March. Strong wet biases are obtained with BMJ over NAP during the month of December and while dry bias with KF and GF. The wet bias in all CPSs over the SAP is observed during February and March.

The average mean temperature bias (Figs. 6d–f) over the AP and its sub-regions for individual months indicates that the CPSs in WRF produce a cold bias. A stronger cold bias of about -2 to -4 K in GF, about -0.5 to -3K in BMJ and about -0.2 to -2 K with KF is obtained in all months. Overall, the results indicate that the KF leads to better simulations of mean surface temperatures. Similar biases are also obtained for maximum and minimum temperatures. From Table 2, the regional temperatures error statistics suggest lower errors and highest correlations with KF.

3.6 Assessment of circulation patterns

Fig. 7 shows the spatial distribution of seasonal mean winter wind flow and geopotential height patterns at 850 hPa from MERRA-2, and WRF with KF, BMJ, and GF. The results shows the salient winter circulation patterns of AP, such as the strong anticyclonic circulation pattern (clockwise rotation) between the central to SAP (referred to as the Arabian anticyclone), the strong westerly winds passing through the Mediterranean Sea towards the NAP, the more pronounced

Accepted for publication in *Journal of Hydrometeorology*. DOI 10.1175/JHM-D-19-0114.1.

wind circulation from the Arabian Gulf to the central AP and NAP, and the RSCZ over the central Red Sea (with its eastern plank towards the AP and its western plank that has moved towards the Sudan region). The geopotential height 850 hPa also indicates the presence of the Arabian anticyclone (high geopotential heights) over the eastern AP, which is an important modulator of rainfall in the region (e.g. Dasari et al., 2018).

The Arabian anticyclonic pattern is well simulated by KF (Fig. 7b) and BMJ (Fig. 7c), although slightly shifted westward in BMJ (Fig. 7a), while GF (Fig. 7d) misses its location as compared to MERRA-2. BMJ- and KF-simulated winds over the Gulf of Aden are in good agreement with MERRA-2, but GF overestimates these winds. KF yields a more realistic simulation of the Arabian anticyclone, RSCZ, and westerly winds. It also shows the southerly flow from the Arabian Sea towards land in agreement with MERRA-2 flow patterns. The mid-level winds (500 hPa) during winter (not shown) from MERRA-2 show a strong anticyclonic circulation over the southern Red Sea and the Sudan region, and these are better simulated by KF and BMJ compared to GF. Over the northern AP, strong mid-tropospheric westerlies are observed in both KF and BMJ, and MERRA-2, which act as wave guides for the Mediterranean westerly systems to generate rainfall over the eastern AP and NEAP.

The seasonal mean distribution of sea level pressure (SLP) during winter (not shown) exhibits low pressure systems over east Africa (the Sudan low) and the south western AP (including the southern Red Sea), and a high pressure system over the NEAP. This meridional pressure gradient (~5 hPa) plays an important role in the generation of the AP winter rainfall. Rainfall in the southwestern AP is developed by the penetration of the low-pressure system emanating from the Sudan low and the Red Sea low, which interacts with the southwestern AP mountains and trigger rainfall (e.g. Chakraborty et al., 2006, Dasari et al., 2018). These winter

Accepted for publication in *Journal of Hydrometeorology*. DOI 10.1175/JHM-D-19-0114.1.

pressure patterns are well simulated by KF, BMJ, GF compared to MERRA-2, while the Sudan lows are better simulated by KF.

The upper tropospheric winds (200 hPa) from MERRA-2, KF, BMJ, and GF (Fig. 7e–h) show the presence of the subtropical westerly jet (SWJ) over the AP, which has highest regional wind speeds of approximately 45 ms^{-1}. This jet is often referred to as the Middle-East jet stream, and is an important dynamical precipitation factor in the AP, acting as a wave guide for westerly disturbances (e.g. Athar et al., 2014; Kumar et al., 2016; Dasari et al., 2018; Attada et al., 2019a). The position and intensity of the upper tropospheric circulation are well simulated by KF and BMJ, whereas GF simulates a northward shifted SWJ compared to MERRA-2. The upper tropospheric geopotential height patterns indicate that the north–south gradient in geopotential height over the AP is better simulated by KF (Fig. 7f) compared to BMJ and GF.

In the upper troposphere, synoptic transients (western disturbances) are pronounced during winter, and these have a significant impact on AP winter rainfall (Yadav et al., 2013; Kang et al., 2015; Almazroui et al., 2016c; Attada et al., 2019a; Dasari et al., 2020). These eastward-moving systems are a result of baroclinic and barotropic energy sources that are generally guided by upper tropospheric jet streams centered between 25°N and 35°N (e.g. Hoell et al., 2015). We thus investigated the sensitivity of synoptic transients during winter to the CPSs over the period 2001–2016. The synoptic variability is shown in terms of 2–8-day filtered upper-level zonal winds. Meridional winds during winter are a good indicator for upper level synoptic transient activity (Fig. 8) (Barlow et al. 2015). In MERRA-2 (Fig. 8a), the mean synoptic transients during winter in the zonal and meridional wind components are pronounced over the NAP and Arabian Gulf during the entire study period. These transients are relatively low in the SAP compared to the NAP. KF (Fig. 8b) and BMJ (Fig. 8c) are better able to produce synoptic transients as compared to

Accepted for publication in *Journal of Hydrometeorology*. DOI 10.1175/JHM-D-19-0114.1.

MERRA-2, while the locations of these transients in GF (Fig. 8d) are shifted northward, associated with the northward shift in the GF-simulated subtropical westerly jet.

We further analyzed the storm tracks to examine the influence of Mediterranean storms on the AP winter rainfall. Figure 9 plots the storm tracks based on the local vorticity maxima at 850 hPa level (Flaounas et al., 2014) as extracted from WRF simulations with KF, BMJ, and GF and compared with the corresponding tracks from MERRA-2. Both model simulations and reanalysis fields show that most of the storm tracks originate in the Mediterranean Sea and propagate eastward before dissipating over the northern AP. These storm passages confirm their important contribution to the rainfall over the AP. The simulation of these storm tracks with KF is relatively in closer agreement with MERRA2 than BMJ and GF. Note that the storms simulated by WRF that originate over the Red Sea region and propagate northward are not observed in the reanalysis. These convective storms, triggered by the RSCZ that form over the central Red Sea move inland into AP. The horizontal length scales of these storms are about 3-5km and require a high resolution model to properly simulate these features. Our high resolution configuration is able to reproduce these small-scale convective activities and their propagation toward the AP. Overall, the intrusion of midlatitude synoptic transients towards the AP, in conjunction with the low-level northward advection of warm and moist air from the Red Sea and Arabian Sea, prompts the dynamic and thermodynamic instabilities to enhance rainfall during winter (e.g. Chakraborty et al., 2006; Kumar et al., 2015; De Vries et al., 2016; Dasari et al., 2019), and this is realistically produced by KF.

3.7 Analysis of moisture distribution and its dynamics

The distribution of moisture and its dynamics are key factors determining the variability of rainfall and characterizing the vertical distribution of specific humidity is crucial for understanding moist

Accepted for publication in *Journal of Hydrometeorology*. DOI 10.1175/JHM-D-19-0114.1.

convective processes over the AP (Chakraborty et al., 2006; Babu et al., 2011, 2016; Kang et al., 2015; Dasari et al., 2018). Analysis of different datasets suggests that moisture budgets over the Mediterranean Sea and the Red Sea, have strong links with AP winter rainfall (Jin et al., 2011; Sahin et al., 2015; Dasari et al., 2018; Zolina et al., 2017). Zolina et al. (2017) pointed that the moisture transportation in the surface layer is dominated by breezes driven by SST, and the advection of moisture above the boundary layer is controlled by regional circulation patterns. This section analyzes the characteristics of the mean specific humidity at different tropospheric levels during winter over the AP as simulated by the WRF model with the different CPSs and from MERRA-2 (Fig. 10).

The spatial distribution of low level (850 hPa) specific humidity (Fig. 10a) from MERRA-2 exhibits highest values of approximately 10 $g.kg^{-1}$ over the southern Red Sea, about 5–6 $g.kg^{-1}$ over the SAP (between 10°N and 23°N), and below 3 $g.kg^{-1}$ over the NAP. KF (Fig. 10b) and BMJ (Fig. 10c) reproduce these regional changes in the specific humidity distribution over the AP, while GF underestimates them over the southern Red Sea and SAP regions, in conjunction with the weaker winds (Fig. 10d). All three schemes show the north–south gradient in the lower tropospheric moisture over the Red Sea, but GF provides lower values, particularly over the Arabian Gulf and NEAP. MERRA-2 (Fig. 10e) shows a narrow zone of specific humidity at a pressure level of 500 hPa from east Africa to the northeastern AP through southwestern AP. The highest specific humidity is reached over the southern Red Sea and Sudan regions, whereas the lowest specific humidity is found over the Arabian and Mediterranean regions. KF (Fig. 10f) exhibits a clear maximum specific humidity extending from the equatorial regions and eastern Africa towards the AP, which is typical of tropical plumes over the region (Ziv, 2001; Rubin et al., 2007; Tubi and Dayan, 2014). These tropical plumes are primarily confined to the winter and

Accepted for publication in *Journal of Hydrometeorology*. DOI 10.1175/JHM-D-19-0114.1.

contribute to the light to heavy widespread rainfall across arid desert regions like the AP. These plumes follow the southward penetration of mid-latitude troughs that are associated with an intensified thermal wind and longer jet streaks (e.g. Tubi and Dayan, 2014). BMJ (Fig. 10g) also simulates these atmospheric plumes of specific humidity, but significantly underestimates their magnitude. GF (Fig. 10h) fails to simulate the mid-tropospheric specific humidity band. Moisture availability in the GF is therefore meager, which results in a dry bias in the precipitation simulation in the NAP. The comparison between the simulated upper tropospheric (200 hPa) specific humidity with MERRA-2 (Figs. 10i-10l) indicates an increased moisture content in KF compared to BMJ and GF. This is due to the higher values of extended specific humidity plumes from the equatorial regions and eastern Africa towards the AP in KF. It also shows that most of the moisture is confined to the SAP and southern Red Sea regions compared to the NAP during winter.

To investigate the moisture source that triggers moist convection and associated rainfall over the AP, the composite winter means of vertically integrated (from the surface to 400 hPa) moisture transport from the model simulations and MERRA-2 are analyzed and presented in Fig. 11, where the vectors represent the resultant moisture transport components of zonal and meridional moisture components. MERRA-2 shows that the moisture fluxes occur predominantly over the Arabian Sea and Red Sea and are driven by the Arabian anticyclone (Fig. 11a). Furthermore, the subtropical jet is associated with an anticyclonic flow over the south of the AP, which advects moisture from the Red Sea and the Arabian Sea. MERRA-2 suggests that moisture originates in the Arabian Sea, Gulf of Aden, and the southern Red Sea as a result of the formation of the Arabian Anticyclone and the effect of the Indian winter monsoon flow (Dasari et al., 2018). It can be discerned that a significant amount of moisture is transported by the westerly winds from the eastern Mediterranean towards the NAP region. Compared to MERRA-2, KF (Fig. 11b)

Accepted for publication in *Journal of Hydrometeorology*. DOI 10.1175/JHM-D-19-0114.1.

provides a more realistic representation of moisture transport and the location of maximum moisture transport (more than 130 Kg $m^{-1}s^{-1}$) over the southern Red Sea and the Gulf of Aden. The model simulations with different CPSs confirm that the Red Sea is a major contributor of moisture for the AP precipitation (Zolina et al., 2017; Dasari et al., 2018; Sandeep and Ajayamohan 2018). The BMJ (Fig. 11c) simulates a similar vertical integrated moisture transport structure to KF and MERRA-2, but with a weaker magnitude. The BMJ also shows that moisture from the southern Red Sea is advected towards eastern Africa. In contrast, GF (Fig. 11d) fails to simulate the locations of maximum moisture transport, and both GF and BMJ display weaker moisture transport flux vectors compared to KF and MERRA-2, which leads to a dry bias in rainfall (Fig. 6). Our analysis of the vertically integrated horizontal moisture fluxes suggests that the availability of higher moisture during winter provides a favorable condition for generating rainfall over the AP and is also associated with weather disturbances migrating from the Mediterranean region. Therefore, proper representation of the sources of moisture in the model is essential to properly resolve the mechanisms for developing moist convection and the associated dynamics of precipitation over the AP. KF and BMJ successfully reproduce these features while GF fails to do so.

4. Vertical structures of dynamic and thermodynamic profiles

This section evaluates the three-dimensional representation of the atmosphere in the model to understand the winter dynamics. Specifically, it focuses on the vertical profiles of temperature and moisture that are interrelated with convective processes, which are essential for initiating convective activity (e.g. Raju et al., 2015a; Martínez-Castro et al., 2017). The representation of these profiles in the model is determined by the convective schemes and is connected with the precipitation formation process.

Accepted for publication in *Journal of Hydrometeorology*. DOI 10.1175/JHM-D-19-0114.1.

Seasonally averaged vertical profiles of different variables were averaged over the NAP (with respect to the highest precipitation in a sub-region) from MERRA-2, KF, BMJ, and GF, and the results are presented in Fig 12. In general, the vertical distribution of temperature decreases with height in MERRA-2 and the model with the three CPSs (Fig 12a). However, KF and BMJ agree better with MERRA-2, albeit for cold biases in the lower troposphere, while GF exhibits a strong cold bias in the lower troposphere and a warm bias in the middle to upper troposphere. Overall and compared to MERRA-2, the temperature distribution in KF is slightly better than that of BMJ and is far superior to that of GF. Warm temperature biases in the upper troposphere are systematically stronger in GF, consistent with weak/scanty rainfall amounts.

The seasonally averaged vertical profile of specific humidity over the NAP (Fig. 12b) shows high magnitudes at the surface (about 6.5 $g.kg^{-1}$) and a gradual decrease with height thereafter. The vertical variations in specific humidity are well simulated by the model with all CPSs. KF exhibits higher moisture in the lower troposphere compared to MERRA-2, whereas BMJ is dry at the surface and in the mid to upper troposphere; however, its results are in good agreement with MERRA-2 in the lower troposphere. GF configuration exhibits a dry bias of approximately 2 $g.kg^{-1}$ in the entire troposphere over the AP, which is further corroborated by the underestimation of rainfall. Compared to the other schemes, the vertical profile configuration of KF is overall closer to that of MERRA-2.

The vertical distribution of zonal winds shows lower tropospheric weak westerlies and mid-to-upper tropospheric strong westerlies over the NAP (Fig. 12c). The highest zonal wind speed (45 ms^{-1}) occurs at 200 hPa over the NAP and is associated with the subtropical westerly jet. This vertical zonal wind structure in KF agrees better with that of MERRA-2 than BMJ and GF, where BMJ simulates stronger zonal wind speeds at 200 hPa and GF underestimates the zonal

Accepted for publication in *Journal of Hydrometeorology*. DOI 10.1175/JHM-D-19-0114.1.

wind in the entire troposphere. These results suggest that the BMJ (GF) simulated zonal wind is strongly (weakly) driven by the subtropical jet. The mean vertical profile of the relative vorticity from MERRA-2 (Fig. 12d) shows a cyclonic circulation (positive values) in the upper troposphere (from 600 hPa to 100 hPa) and an anticyclonic circulation (negative values) in the surface to the middle troposphere (from surface to 600 hPa). In KF, a low-level anticyclonic vorticity and cyclonic vorticity aloft is noticeable, in agreement with the observations. The relative vorticity profile is also reproduced by BMJ, but with considerable discrepancies compared to MERRA-2, while the results of GF are completely offset from the observations, except at the surface.

The time-averaged vertical distributions of diabatic heating over the north Arabian Peninsula (NAP) region from MERRA-2 and WRF simulations with KF, BMJ and GF are shown in Figure 12e. MERRA-2 shows maximum diabatic heating in the lower (upper) troposphere below 900 hPa (above 150 hPa), whereas strong diabatic cooling with two maxima in the middle troposphere (between 900 to 150 hPa), indicating the dominance of radiative cooling. KF, BMJ and GF simulated similar vertical structures of diabatic heating as those of MERRA-2, but not in terms of magnitudes. As compared to BMJ and GF, the vertical profile of apparent heat source from KF is in better agreement with MERRA-2. GF shows a large deviation in the vertical profile compared to MERRA-2, with a maximum surface heating and strong diabatic cooling in the upper troposphere. Discrepancies in representing the diabatic heating profile by BMJ and GF lead to discrepancies in instability, and in turn precipitation biases. These profiles are qualitatively similar to those reported in earlier studies (e.g. Shay-El and Alpert, 1991).

4.1 Evaluation of cloud distribution

In this section, we evaluate the efficiency of different convective schemes in representing different cloud types. Clouds are evidently important for providing the precipitation distribution (e.g. Diaz

Accepted for publication in *Journal of Hydrometeorology*. DOI 10.1175/JHM-D-19-0114.1.

et al., 2015) and cloud processes are often poorly represented in numerical models (e.g. Randall et al., 2003; Stevens and Bony, 2013). We present different cloud levels (low, middle and high clouds) during winter from CERES observations along with those from the model simulations using the three different CPSs (Fig. 13).

Observations (Fig. 13a) indicate that a high percentage (more than 25%) of low-level clouds (which have a cloud-top height below 700 hPa level) are located over the southern and central Red Sea, Mediterranean Sea, Arabian Gulf, and the Gulf of Aden. Other parts of the Red Sea and the NAP show a 10% to 20 % coverage of low-level clouds. 10%–15% of low-level clouds are distributed over the NAP and NEAP regions, and low-level cloud coverage is limited over the land regions of the SAP. This indicates that most of the low-level clouds over the Red Sea are associated with the RSCZ, which is a shallow system that creates maritime stratocumulus clouds, and this is also observed over the Arabian Gulf and the Mediterranean Sea. KF (Fig. 13b) and BMJ (Fig. 13c) are able to well simulate the low-level cloud distribution, slightly underestimated, over the Red Sea and AP. Although GF captures the correct low-level cloud over the RSCZ and Arabian Gulf regions, it fails to simulate the low-level clouds in the NAP (Fig. 13d). All the schemes fail to reproduce the observed cloud structure in the SAP.

The observed middle clouds over the region with cloud-top heights between 350 hPa and 700 hPa levels (Fig. 13e) show maximum cloud coverage over the NAP region (> 10%–15 %), while the SAP is not covered by these alto-stratus cloud types. KF (Fig. 13f) and BMJ (Fig. 13g) provide a proper representation of mid-level clouds over the NAP, but with excess coverage compared to MERRA-2, whereas GF fails to produce these mid-level clouds and confines them to the far north of the domain. Overall, KF simulates a north–south distribution of mid-level clouds that is more in agreement with the observations than the other two CPSs. High-level clouds from

Accepted for publication in *Journal of Hydrometeorology*. DOI 10.1175/JHM-D-19-0114.1.

MERRA-2 (Fig. 13i) show less amount of cirrus clouds compared to low- and mid-level clouds during winter, whereas KF (Fig. 13j) and BMJ (Fig. 13k) simulated more high-level clouds compared to the observations. This is more noticeable over the SAP for GF, which simulates high values of cloud coverage. GF results over the NAP well match the observed high-level clouds during winter. However, the locations of high clouds are better depicted by KF and BMJ, as compared to MERRA-2. Overall, KF and BMJ outperform GF in simulating the low and mid-level clouds, but they struggle with the simulation of high-level clouds during winter over the AP.

4.2 Vertical distribution of cloud microphysical properties

The vertical structures of cloud hydrometeors have a large impact on precipitation processes (e.g. Rajeevan et al. 2013), and are thus investigated here. We focus in particular on the cloud microphysical properties over the NAP, which receives the largest amount of rainfall.

The vertical profiles of liquid hydrometeors (cloud and rain water) and solid hydrometeors (graupel, ice, and snow) over the NAP are presented in Fig. 14. Because of the lack of data, the validation of the model-simulated hydrometeors is only conducted for cloud water and ice mixing ratio profiles using MERRA-2. The results suggest an increase in cloud water from the surface to 700 hPa, and thereafter a decrease with height in both MERRA-2 and the model simulations. The main cloud deck (maximum peak of cloud water mixing ratio) is located at 700 hPa in KF and BMJ, is in agreement with the observations (Fig. 14a). KF shows slightly higher values of cloud water than BMJ, while GF fails to produce cloud water, leading to a significant underestimation and shift of the maxima to lower levels at around 900 hPa.

The vertical profile of the rain water maxing ratio (Fig. 14b) suggests that the maximum amount of rain water is available at a pressure level of 750 hPa (slightly below cloud water) in both KF and BMJ. Raindrops are the only precipitating hydrometeor at the lowest level of the

Accepted for publication in *Journal of Hydrometeorology*. DOI 10.1175/JHM-D-19-0114.1.

atmosphere as can be seen in Fig. 14(b) for both BMJ and KF. The rain water mixing ratio produced from GF is different than that of KF and BMJ. For the graupel mixing ratio (Fig. 14c), BMJ simulates the maximum peak at 650 hPa reasonably well, whereas GF fails to achieve this. The ice mixing ratio (Fig. 14d) has a maximum peak at 300 hPa (above the freezing level), which is more underestimated in BMJ than in KF. GF fails to distribute the ice mixing ratio over the NAP. All CPSs leads to a significant underestimation of cloud ice compared to MERRA-2. The ice hydrometeor profile is the key microphysical processes in the formation of precipitation. As the ice crystals grows, they become heavier than snow particles before they start falling, which leads to growth of graupel by accretion of supercooled water and then melt just above the surface to form rainfall (e.g. Gao et al., 2016). Although KF underestimates this process, it performs slightly better than BMJ and GF. The failure of BMJ and GF in reproducing this important process could be one of the reasons for their simulated dry rainfall biases over the AP. The vertical profile of the snow mixing ratio (Fig. 14e) indicates that the upper troposphere (450 hPa) is characterized by the maximum amount of snow, with KF exhibiting a higher snow mixing ratio than BMJ and GF. It is thus assumed that the sources of systematic model errors (in Figure 14) are related to the cloud modeling in the different convective schemes, including the model vertical resolution.

Overall, liquid hydrometers are formed below the freezing level where warm precipitation processes occur, and ice, graupel, and snow are distributed beyond the freezing level and are mainly related to cold precipitation processes over the AP. Therefore, an improved representation of the vertical structure of cloud hydrometeors is necessary for providing realistic model simulations of AP winter rainfall; this is not actualized in GF, which results in a poorer rainfall simulation skill than BMJ and KF.

Accepted for publication in *Journal of Hydrometeorology*. DOI 10.1175/JHM-D-19-0114.1.

5. Summary and Conclusions

This study evaluated the performance of the WRF model and its sensitivity to three CPSs (Kain-Fritsch (KF), Betts-Miller-Janjic (BMJ) and the scale-aware Grell-Freitas (GF)) for seasonal scale simulations of AP winter rainfall during the period 2001 to 2016, and then elucidated the associated regional dynamics. We used WRF model configured on two two-way nested domains with respective horizontal resolutions of 15 km and 5 km to capture the detailed rainfall distribution and associated underlying processes. The model simulated variables were validated against satellite observations and reanalysis datasets, before investigating the sensitivity of the three CPSs.

Our results suggest that the model-simulated seasonal scale AP winter rainfall is sensitive to the CPSs. KF appears to produce realistic geographic distributions, and its simulated seasonal climatology of precipitation and air temperature are in good agreement with the observations compared to BMJ and GF. All CPSs exhibit, however, dry biases in rainfall and cold biases in mean, maximum, and minimum 2-m temperatures. Overall, KF depicts higher spatial correlations with less errors for temperature (including maximum and minimum) and precipitation compared to BMJ and GF. Furthermore, the standard deviation of temperature and precipitation are also better reproduced by KF; while BMJ produces better variability than GF (on par with KF) over some parts of the AP. The analysis of daily mean regional precipitation indicates that BMJ and GF fail to well reproduce the seasonal evolution of rainfall compared to the observations and KF. Precipitation over the AP is better captured by KF albeit with a slight underestimation.

The Arabian anticyclone, which is one of the main characteristics of low-level circulation, is well captured by KF and BMJ, but its position is shifted in GF. Strong westerly winds passing through the Mediterranean Sea towards the NAP and the winds blowing from the Arabian Gulf to the central and NAP regions are better simulated by KF than by BMJ and GF. In the case of upper

Accepted for publication in *Journal of Hydrometeorology*. DOI 10.1175/JHM-D-19-0114.1.

tropospheric circulation, KF and BMJ simulate well the SWJ (in terms of location and strength) as compared to MERRA-2. The position of SWJ is important and acts as a waveguide for westerly disturbances and associated precipitation in the AP. Overall, KF is better able to represent the eastward moving storm systems (large scale synoptic transients and storm tracks) that are guided by the SWJ. The proper representation of moisture sources in KF enables the development of moist convection and associated precipitation dynamics in the AP; both BMJ and GF generally fail to simulate these structures.

The simulated vertical profiles of several atmospheric variables, such as temperature, specific humidity, zonal wind, and relative vorticity were also evaluated, suggesting that the KF exhibits higher fidelity with the observed atmospheric structures compared to BMJ and GF, which leads to better vertical thermodynamic structures and realistic convective precipitation. The discrepancies between the different schemes reveal that the proper simulation of different cloud types and associated cloud hydrometer responses enables KF to better simulate the rainfall variability over the AP.

This study examined the differences between the three CPSs in terms of simulating the AP winter rainfall, but did not attempt to determine which processes within the schemes produce the differences outlined here. Liang et al. (2004) suggested that the KF incorporates detailed cloud microphysics and entrainment and detrainment between clouds and environment, which are not described in the two other convective schemes. Moreover, sub-grid scale cloud-radiation interactions within the KF have been found to be important (Alapaty et al., 2012; Herwehe et al., 2014) in the simulation of precipitation. The analysis of heat source (diabatic heating) suggests that KF more accurately simulates the thermodynamic feedback to rainfall. This further improves the representation of the vertical structure of cloud hydrometeors, which in turn better resolves the

Accepted for publication in *Journal of Hydrometeorology*. DOI 10.1175/JHM-D-19-0114.1.

precipitation distribution. Further, the superiority of the KF can also be explained by its appropriate treatment of convective available potential energy as a triggering function, and its treatment of deep convection with strong updrafts, downdrafts, and environmental mass fluxes that adjust precipitation. It should also be noted that the difficulties in accurately simulating AP precipitation could be caused by deficiencies in other related physical processes, such as the subtropical westerly jet, synoptic transients, and cloud microphysics (Dai and Trenberth, 2004). Based on the results of our study, GF seem to be relatively less suitable for simulation of AP rainfall with WRF.

Our study investigated the sensitivity of winter rainfall over the AP with respect to the convective parametrization schemes within a high-resolution (5 km) regional modeling framework. Several other studies advocated for the use of CPSs at this resolution, suggesting improved simulations compared to fully explicit simulations (e.g. McMillen and Steenburgh, 2015; Lind et al. 2016). Convective resolving models were not investigated yet for predicting the AP rainfall; this will be investigated in our future work. Note that the treatment of dust in the model may play an important role in the simulation of AP rainfall through the aerosol-radiative feedback mechanisms. The complex interaction processes between aerosols and rainfall will also be investigated in our future work.

Acknowledgments

This research work was supported by the Office of Sponsored Research (OSR) at King Abdulla University of Science and Technology (KAUST) under the “Virtual Red Sea Initiative” (Grant # REP/1/3268-01-01). All simulations were conducted on the KAUST Super Computational facility SHAHEEN supported by the KAUST Supercomputing Laboratory (KSL). The authors would like to thank three anonymous reviewers for their constructive and insightful comments.

Accepted for publication in *Journal of Hydrometeorology*. DOI 10.1175/JHM-D-19-0114.1.

References

Abid, M.A, F. Kucharski, M. Almazroui, and I. Kang, 2016: Interannual rainfall variability and ECMWF-Sys4-based predictability over the Arabian Peninsula winter monsoon region. Q. J. R. Meteorol. Soc. 142(694):233–242.

Alapaty, K., J. A. Herwehe, T. L. Otte, C. G. Nolte, O. R. Bullock, M. S. Mallard, J. S. Kain and J. Dudhia, 2012: Introducing subgrid-scale cloud feedbacks to radiation for regional meteorological and climate modeling. Geophys. Res. Lett., 39, L24809, https://doi.org/10.1029/2012 GL054031.

Almazroui, M., 2016a: RegCM4 in climate simulation over CORDEX-MENA/Arab domain: selection of suitable domain, convection and land surface schemes. Int. J. Climatol., 36, 236–351 http://dx.doi.org/10.1002/joc.4340.

Almazroui, M, M. N. Islam, A. K. Al-Khalaf and F. Saeed, 2016b: Best convective parameterization scheme within RegCM to downscale CMIP5 multi-model data for the CORDEX-MENA/Arab domain. Theor. Appl. Climatol., 124, 807–823, https://doi.org/10.1007/s00704-015-1463-5

Almazroui, M., S. Kamil, K. Ammar, K. Keay, A.O. Alamoudi, A, 2016c. Climatology of the 500-hPa Mediterranean storms associated with Saudi Arabia wet season precipitation. Climate Dynamics, 48, 3309–3324.

Almazroui, M., R. Dambul, N.Islam and P. J. Jones, 2015: Atmospheric circulation patterns in the Arab region and its relationships with Saudi Arabian surface climate: a preliminary assessment. Atmos. Res., 161−162, 36−51, https://doi.org/10.1016/j.atmosres.2015.03.014.

Almazroui, M., M. Adnan Abid, H. Athar, M. Nazrul Islam and M. Azhar Ehsan, 2013: Interannual variability of rainfall over the Arabian Peninsula using the IPCC AR4 Global Climate Models. Int. J. Climatol., 33 (10), 2328-2340, https://doi.org/10.1002/joc.3600.

Accepted for publication in *Journal of Hydrometeorology*. DOI 10.1175/JHM-D-19-0114.1.

Almazroui, M., 2012: Dynamical downscaling of rainfall and temperature over the Arabian Peninsula using RegCM4, Climate Research, 52, 49-62, doi:10.3354/cr01073.

Almazroui, M., 2011: Calibration of TRMM rainfall climatology over Saudi Arabia during 1998–2009. Atmos. Res., 99: 400– 414, https://doi.org/10.1016/j.atmosres.2010.11.006.

Arakawa, A., J. H. Jung, and C. M. Wu, 2011: Toward unification of the multiscale modeling of the atmosphere. Atmos. Chem. Phys., 11, 3731–3742, https://doi.org/10.5194/acp-11-3731-2011.Arakawa, A., and W. H. Schubert, 1974: Interaction of a cumulus cloud ensemble with the large-scale environment, Part I. *J. Atmos. Sci.*, **31,** 674–701.

Argüeso D, J.M. Hidalgo-Muñoz, S.R. Gámiz-Fortis, M. J. Esteban-Parra, J. Dudhia, and Y. Castro-Diez 2011. Evaluation of WRF parameterizations for climate studies over Southern Spain using a multistep regionalization. J Clim 24:5633–5651. doi:10.1175/JCLI-D-11-00073.1

Athar, H., 2014: Trends in observed extreme climate indices in Saudi Arabia during 1979–2008. Int. J. Climatol., 34, 1561–1574. Doi: 10.1002/joc.3783.

Attada R., H.P. Dasari, A. Parekh, J. S. Chowdary, S. Langodan, O. Knio, and I. Hoteit, 2019a: The role of the Indian Summer Monsoon variability on Arabian Peninsula summer climate. Clim Dyn., 52, 3389, doi: 10.1007/s00382-018-4333-x.

Attada, R., H. P. Dasari, J. S. Chowdary, Y. Ramesh Kumar, O. Knio, and I. Hoteit, 2019b: Surface air temperature variability over the Arabian Peninsula and its links to circulation patterns. Int. J. Climatol., 39(1), 445-464, https://doi.org/10.1002/joc.5821.

Attada, R., K. Ravi Kumar, Y. Ramesh Kumar, H. P. Dasari, O. Knio, and I. Hoteit, 2018: Prominent modes of summer surface air temperature variability and associated circulation anomalies over the Arabian Peninsula. Atmos. Sci. Lett., 19:e860, https://doi.org/10. 1002/asl.860.

Accepted for publication in *Journal of Hydrometeorology*. DOI 10.1175/JHM-D-19-0114.1.

Babu, C.A., P. R. Jayakrishnan, and H. Varikoden, 2016: Characteristics of precipitation pattern in the Arabian Peninsula and its variability associated with ENSO. Arab. J. Geosci., 9, 186. https://doi.org/10.1007/s12517-015-2265-x.

Babu, C.A., A. A. Samah, and H. Varikoden, 2011: Rainfall climatology over Middle East Region and its variability. Int. J. Water Resour. Arid Environ 1(3), 180–192.

Barlow, M., B. Zaitchik, S. Paz, E. Black, J. Evans, and A. Hoell, 2015: A review of drought in the Middle East and southwest. Asia. J. Clim. 29, 8547-8574, doi: 10.1175/JCLI-D-13-00692.1.

Bennett, L. J., and Coauthors, 2011: Initiation of convection over the Black Forest mountains during COPS IOP15a.Q. J. R. Meteor. Soc.,137, 176–189. https://doi.org/10.1002/qj.760.

Betts, A. K., and M.J. Miller, 1986: A new convective adjustment scheme. Part II: Single column tests using GATE wave, BOMEX, and arctic air-mass data sets. Q. J. R. Meteor. Soc., 112 (473), 693–709, https://doi.org/10.1002/qj.49711247308.

Bhomia, S., P. Kumar and C.M. Kishtawal, 2019: Evaluation of the Weather Research and Forecasting Model Forecasts for Indian Summer Monsoon Rainfall of 2014 Using Ground Based Observations, Asia-Pacific J Atmos Sci (2019) 55: 617. https://doi.org/10.1007/s13143-019-00107-y.

Chakraborty, A., S.K. Behera, M. Mujumdar, R. Ohba, and T. Yamagata, 2006: Diagnosis of tropospheric moisture over Saudi Arabia and influences of IOD and ENSO. *Mon. Wea. Rev.*, **134,** 598–617.

Chen, F., and J. Dudhia, 2001: Coupling an advanced land surface–hydrology model with the Penn State–NCAR MM5 modeling system. Part I: Model implementation and sensitivity. *Mon. Wea. Rev.*, **129,** 569–585.

Accepted for publication in *Journal of Hydrometeorology*. DOI 10.1175/JHM-D-19-0114.1.

Crétat, J., B. Pohl, Y. Richard, and P. Drobinski, 2012: Uncertainties in simulating regional climate of Southern Africa: sensitivity to physical parameterizations using WRF. Clim. Dyn., 38, 613−634, https://doi.org/10.1007/s00382-011-1055-8.

Dai, A., and K. E. Trenberth, 2004: The diurnal cycle and its depiction in the Community Climate System Model. *J. Climate*, **17,** 930–951.

Dasari, H. P., D. Srinivas, S. Langodan, R. Attada, A. Karumuri, and I. Hoteit, 2020: The long-term changes of the Arabian Peninsula Rainfall and its Relationship with the ENSO signals in the Tropical Indo-Pacific. Under review J. Climate.

Dasari, H.P, D. Srinivas, S. Langodan, R. Attada, R. K. Kunchala, V. Yesubabu, K. Omar and I. Hoteit, 2019: A High-Resolution Assessment of Solar Radiation Resources for the Arabian Peninsula" Applied Energy, 248, 354-371.

Dasari, H.P., S. Langodan, Y. Viswanadhapalli, B. R. Vadlamudi, V. P. Papadopoulos, and I. Hoteit, 2018: ENSO influence on the interannual variability of the Red Sea convergence zone and associated rainfall. Int. J. Climatol, 38, 761–775. doi:10.1002/joc.5208.

De Vries, A. J., S. B. Feldstein, M. Riemer, E. Tyrlis, M. Sprenger, M. Baumgart, M. Fnais, and J. Lelieveld, 2016: Dynamics of tropical–extratropical interactions and extreme precipitation events in Saudi Arabia in autumn, winter and spring. Q. J. R. Meteor. Soc., 142,1862–1880, https://doi.org/10.1002/qj.2781.

De Vries, A. J., E. Tyrlis, D. Edry, S. O. Krichak, B. Steil, and J. Lelieveld, 2013: Extreme precipitation events in the Middle East: Dynamics of the Active Red Sea Trough, J. Geophys. Res. Atmos., 118, 7087–7108, doi:10.1002/jgrd.50569.

Díaz, J.P., A. González, F. J. Expósito, J. C. Pérez, J. Fernández, M. García-Díez, and D. Taima, 2015: WRF multi-physics simulation of clouds in the African region. Q. J. R. Meteorol. Soc., 141, 2737 – 2749, October 2015 A, doi:10.1002/qj.2560.

Accepted for publication in *Journal of Hydrometeorology*. DOI 10.1175/JHM-D-19-0114.1.

Ehsan, M.A., M. Almazroui, A. Yousef, O. B. Enda, M. K. Tippett, F. Kucharski, and A. K. Alkhalaf, 2017: Sensitivity of AGCM simulated regional summer precipitation to different convective parameterizations. Int. J. Climatol., 37,4594–4609, https://doi.org/10.1002/joc.5108.

Evans, J. P., M. Ekström, and F. Ji, 2012: Evaluating the performance of a WRF physics ensemble over South-East Australia. Climate Dyn., 39, 1241–1258, doi:10.1007/s00382-011-1244-5.

Evans, J. P., R. B. Smith, and R. J. Oglesby, 2004: Middle East climate simulation and dominant precipitation processes. Int J Climatol 24:1671–1694.

Flaounas, E., V. Kotroni, K. Lagouvardos, and I. Flaounas, 2014: CycloTRACK (v1.0)—tracking winter extratropical cyclones based on relative vorticity: Sensitivity to data filtering and other relevant parameters. Geoscientific Model Development, 7, 1841–1853.

Fritsch, J. M. and C. F. Chappell. 1980. Numerical prediction of convectively driven mesoscale pressure systems. Part I: Convective parameterization. J. Atmos. Sci. 37:1722–1733.

Gao, W., C.-H. Sui, J. Fan, Z. Hu, and L. Zhong, 2016: A study of cloud microphysics and precipitation over the Tibetan Plateau by radar observations and cloud-resolving model simulations. J. Geophys. Res. Atmos., 121(22), 13735– 13752, https://doi.org/10.1002/2015JD024196.

Gao, Y., R. Leung, C. Zhao, and S. Hagos, 2017: Sensitivity of U.S. summer precipitation to model resolution and convective parameterizations across gray zone resolutions. J. Geophys. Res. Atmos., 122, 2714– 2733, https://doi.org/10.1002/2016JD025896.

Gelaro, R. et al, 2017. The modern-era retrospective analysis for research and applications, version 2 (MERRA-2). *J. Clim.* **30**, 5419–5454 .

Giorgi, F., and L. O. Mearns, 1999: Introduction to special section: regional climate modeling revisited. J. Geophys. Res., 104(D6), 6335– 6352, https://doi.org/10.1029/98JD02072.

Accepted for publication in *Journal of Hydrometeorology*. DOI 10.1175/JHM-D-19-0114.1.

Grell, G. A., and S. R. Freitas, 2014: A scale and aerosol aware stochastic convective parameterization for weather and air quality modeling. Atmos. Chem. Phys., 14(10), 5233–5250, https://doi.org/10.5194/acp-14-5233-2014.

Grell, G. A., and D. Dévényi, 2002: A generalized approach to parameterizing convection combining ensemble and data assimilation techniques. Geophys. Res. Lett., 29(14), 1693, doi:10.1029/2002GL015311.

Grell, G. A. 1993: Prognostic evaluation of assumptions used by cumulus parameterizations. Mon. Wea. Rev. 121:764–787.

Han, J.-Y., S.-Y. Hong, K.-S. S. Lim, and J. Han, 2016: Sensitivity of a cumulus parameterization scheme to precipitation production and its impact on a heavy rain event over Korea. *Mon. Wea. Rev.*, **144**, 2125–2135, https://doi.org/10.1175/MWR-D-15-0255.1.

Hasanean H, and M. Almazroui, 2015: Rainfall: features and variations over Saudi Arabia, a review. Climate 3(3):578–626.

Herwehe, J. A., K. Alapaty, T. L. Spero, and C. G. Nolte, 2014: Increasing the credibility of regional climate simulations by introducing subgrid-scale cloud-radiation interactions. J. Geophys. Res. 119, 5317–5330. https://doi.org/10.1002/2014JD021504.

Hoell, A., C. Funk, and M. Barlow, 2015: The forcing of southwestern Asia teleconnections by low-frequency sea surface temperature variability during boreal winter. *J. Climate*, **28**, 1511–1526, doi:https://doi.org/10.1175/JCLI-D-14-00344.1.

Hong, S.-Y., and J.-O. J. Lim, 2006: The WRF single-moment 6-class microphysics scheme (WSM6). J. Korean Meteor. Soc., 42, 129–151.

Huffman, G. J., R. F. Adler, D. T. Bolvin, and E. J. Nelkin, 2010: The TRMM multi-satellite precipitation analysis (TMPA). *Satellite Rainfall Applications for Surface Hydrology*, F. Hossain and M. Gebremichael, Eds., Springer-Verlag, 3–22.

Accepted for publication in *Journal of Hydrometeorology*. DOI 10.1175/JHM-D-19-0114.1.

Huffman, G. J., and Coauthors, 2007: The TRMM multisatellite precipitation analysis (TMPA): Quasi-global, multiyear, combined-sensor precipitation estimates at fine scales. J. Hydrometeor., 8, 38–55.

Iacono, M. J., J. S. Delamere, E. J. Mlawer, M. W. Shephard, S. A. Clough, and W. D. Collins, 2008: Radiative forcing by long-lived greenhouse gases: Calculations with the AER radiative transfer models. J. Geophys. Res., 113, D13103,doi:https://doi.org/10.1029/2008JD009944.

Janjić, Z. I. 1994. The step-mountain eta coordinate model: Further developments of the convection, viscous sublayer, and turbulence closure schemes. Mon. Wea. Rev. 122:927–945.

Jin, F., A. Kitoh, and P. Alpert, 2011: Climatological relationships among the moisture budget components and rainfall amounts over the Mediterranean based on a super-high-resolution climate model. J. Geophys. Res., 116, D09102, doi: https://doi.org/10.1029/2010JD014021.

Kain, J. S., 2004: The Kain-Fritsch convective parameterization: an update. J. Appl. Meteorol. 43, 170–181, https://doi.org/10.1175/1520-0450(2004)043<0170:TKCPAU>2.0.CO;2.

Kain, J. S., and J. M. Fritsch, 1993: Convective parameterization for mesoscale models: The Kain–Fritsch scheme. The Representation of Cumulus Convection in Numerical Models, Meteor. Monogr., No. 46, Amer. Meteor. Soc., 165–170.

Kala, J., J. Andrys, T. J. Lyons, I. J. Foster, and B. J. Evans, 2015: Sensitivity of WRF to driving data and physics options on a seasonal time-scale for the southwest of Western Australia. Climate Dyn., 44, 633–659, https://doi.org/10.1007/s00382-014-2160-2.

Kang, I. S., I. U. Rashid, F. Kucharski, M. Almouzouri, and A. A. Al-Khalaf, 2015: Multidecadal changes in the relationship between ENSO and wet-season precipitation in the Arabian Peninsula. J. Clim. 28, 4743–4752, doi: 10.1175/JCLI-D-14-00388.1.

Accepted for publication in *Journal of Hydrometeorology*. DOI 10.1175/JHM-D-19-0114.1.

Kumar, K. N., A. Molini, T. B. M. J. Ouarda, and M. N. Rajeevan, 2017: North Atlantic controls on wintertime warm extremes and aridification trends in the Middle East. Sci. Rep., 7, 12301.

Kumar, K. N., T. B. M. J. Ouarda, S. Sandeep, and R.S. Ajayamohan, 2016: Wintertime precipitation variability over the Arabian Peninsula and its relationship with ENSO in the CAM4 simulations. Climate Dyn., 47, 1–12. https://doi.org/10.1007/s00382-016-2973-2.

Kumar, K. N., D. Entekhabi, and A. Molini, 2015: Hydrological extremes in hyperarid regions: A diagnostic characterization of intense precipitation over the Central Arabian Peninsula. J. Geophys. Res. Atmos., 120, 1637–1650. doi: 10.1002/2014JD022341.

Kumar, P., and Munn V. Shukla. 2019: Assimilating INSAT-3D Thermal Infrared Window Imager Observation with the Particle Filter: A Case Study for Vardah Cyclone. Journal of Geophysical Research: Atmospheres 124, no. 4 (2019): 1897-1911.

Lind, P., D. Lindstedt, E. Kjellström, and C. Jones, 2016: Spatial and temporal characteristics of summer precipitation over central Europe in a suite of high-resolution climate models. *J. Climate*, **29**, 3501–3518, doi:https://doi.org/10.1175/JCLI-D-15-0463.1.

Liu, C., and M. W. Moncrieff, 2007: Sensitivity of cloud-resolving simulations of warm season convection to cloud microphysics parameterizations. Mon. Wea. Rev., 135, 2854–2868.

Liang, X-Z., L. Li, K. Kunkel, M. Ting, and J. X. L. Wang, 2004: Regional climate simulations of U.S. precipitation during 1982–2002. Part I: Annual cycle. *J. Climate*, **17,** 3510–3529.

Lucas-Picher, P., and Coauthors, 2011: Can regional climate models represent the Indian monsoon? *J. Hydrometeor.*, **12**, 849–868.

Martínez-Castro, D., A. Vichot-Llano, A. Bezanilla-Morlot, A. Centella-Artola, J. Campbell, F. Giorgi, and C. C. Viloria-Holguin, 2017: The performance of RegCM4 over the Central America and

Accepted for publication in *Journal of Hydrometeorology*. DOI 10.1175/JHM-D-19-0114.1.

Caribbean regions using different cumulus parameterizations. Climate Dyn., 50, 4103–4126. https://doi.org/10.1007/s00382-017-3863-y.

McMillen, J. D., and W. J. Steenburgh, 2015: Capabilities and limitations of convection-permitting WRF simulations of lake-effect systems over the Great Salt Lake. Wea. Forecasting, 30, 1711–1731, https://doi.org/10.1175/WAF-D-15-0017.1.

Mooney, P. A., F. J. Mulligan, and R. Fealy, 2013: Evaluation of the sensitivity of the weather research and forecasting model to parameterization schemes for regional climates of Europe over the period 1990–95. *J. Climate*, **26**, 1002–1017, doi:https://doi.org/10.1175/JCLI-D-11-00676.1.

Mukhopadhyay, P., S. Taraphdar, B. N. Goswami, and K. Krishnakumar, 2010: Indian summer monsoon precipitation climatology in a high-resolution regional climate model: Impacts of convective parameterization on systematic biases. *Wea. Forecasting*, **25**, 369–387, doi:https://doi.org/10.1175/2009WAF2222320.1.

Nakanishi, M., and H. Niino, 2004: An Improved Mellor–Yamada Level-3 Model with Condensation Physics: Its Design and Verification. Boundary-Layer Meteor., 112, 1–31, https://doi.org/10.1023/B:BOUN.0000020164.04146.98.

Osman-Elasha, B., 2010: Mapping of climate change threats and human development impacts in the Arab region. Research Papers Series 03/2010; UNDP, Arab Human Development Report. http://www.arab-hdr.org/publications/other/ahdrps/paper02-en. pdf. Accessed 2nd Mar 2015.

Ouda, K.M.O., 2013: Review of Saudi Arabia Municipal Water Tariff. World Environment, 3(2), 66-70. doi: 10.5923/j.env.20130302.05.

Accepted for publication in *Journal of Hydrometeorology*. DOI 10.1175/JHM-D-19-0114.1.

Prein, A. F., and Coauthors, 2015: A review on regional convection-permitting climate modeling: Demonstrations, prospects and challenges. Rev. Geophys., 53, 323–361, doi:https://doi.org/10.1002/2014RG000475.

Ragab, R, and C. Prudhomme, 2000: Climate change and water resources management in the southern Mediterranean and Middle East countries. In The Second World Water Forum 17–22, March 2000, The Hague.

Rajeevan, M., P. Rohini, K. Niranjan Kumar, J. Srinivasan and C. K. Unnikrishnan, 2013: A study of vertical cloud structure of the Indian summer monsoon using CloudSat data. Climate Dyn., 40,637–650. doi:10.1007/s00382-012-1374-4.

Raju, A., A. Parekh, J. S. Chowdary, and C. Gnanaseelan, 2018: Reanalysis of the Indian summer monsoon: Four dimensional data assimilation of AIRS retrievals in a regional data assimilation and modeling framework. Climate Dyn., 50, 2905–2923. doi:10.1007/s00382-017-3781-z.

Raju, A., A. Parekh, J. S. Chowdary, and C. Gnanaseelan, 2015a: Assessment of the Indian summer monsoon in the WRF regional climate model. Climate Dyn., 44, 3077–3100, https://doi.org/10.1007/s00382-014-2295-1.

Raju, A., A. Parekh, P. Kumar, and C. Gnanaseelan, 2015b: Evaluation of the impact of AIRS profiles on prediction of Indian summer mon- soon using WRF variational data assimilation system. J. Geophys. Res. Atmos., 120, 8112–8131. doi:10.1002/2014JD023024.

Randall, D. A., M. Khairoutdinov, A. Arakawa, and W. Grabowski, 2003b: Breaking the cloud parameterization deadlock. *Bull. Amer. Meteor. Soc*, **84,** 1547–1564.

Ratna, S. B., J. V. Ratnam, S. K. Behera, C. J. de W. Rautenbach, T. Ndarana, K. Takahashi, and T. Yamagata, 2014: Performance assessment of three convective parameterization schemes in

Accepted for publication in *Journal of Hydrometeorology*. DOI 10.1175/JHM-D-19-0114.1.

WRF for downscaling summer rainfall over South Africa. Climate Dyn., 42, 2931–2953, doi: https://doi.org/10.1007/s00382-013-1918-2.

Ratnam, J. V., S. K. Behera, R. Krishnan, T. Doi, and S. B. Ratna, 2017: Sensitivity of Indian summer monsoon simulation to physical parameterization schemes in the WRF model. Climate Res., 74, 43–66, https://doi.org/10.3354/cr01484.

Rubin, S., B. Ziv, and N. Paldor, 2007: Tropical plumes over eastern North Africa as a source of rain in the Middle East. *Mon. Wea. Rev.*, **135**, 4135–4148, https://doi.org/10.1175/2007MWR 1919.1.

Sahin, S., M. Türkes, S.-H. Wang, D. Hannah, and W. Eastwood, 2015: Large scale moisture flux characteristics of the Mediterranean basin and their relationships with drier and wetter climate conditions. Climate Dyn., 45, 3381–3401, https://doi.org/10.1007/s00382-015-2545-x.

Sandeep, S., and R. S. Ajayamohan, 2018: Modulation of winter precipitation dynamics over the Arabian Gulf by ENSO. J. Geophys. Res. Atmos., 123, 198– 210, https://doi.org/10.1002/ 2017JD027263.

Shay-El, Y., and P. Alpert, 1991: A diagnostic study of winter diabatic heating in the Mediterranean in relation to cyclones. Quart. J. Roy. Meteor. Soc., 117, 715–747.

Skamarock, W. C., and Coauthors, 2008: A description of the Advanced Research WRF version 3. NCAR Tech. Note NCAR/TN-475+STR, 113 pp. [Available online at www.mmm.ucar.edu/wrf/users/docs/arw_v3_bw.pdf.]

Srinivas, C. V., H. P. Dasari, D. V. B. Rao, Y. Anjaneyulu, R. Baskaran, and B. Venkatraman, 2013: Simulation of the Indian summer monsoon regional climate using advanced research WRF model. Int. J. Climatol., 33, 1195–1210, https://doi.org/10.1002/joc.3505.

Accepted for publication in *Journal of Hydrometeorology*. DOI 10.1175/JHM-D-19-0114.1.

Stevens, B, and S. Bony, 2013: What are climate models missing?. Science 340, 1053–1054, doi:10.1126/science.1237554.

Sultana, R, and N. Nasrollahi, 2018: Evaluation of remote sensing precipitation estimates over Saudi Arabia. J Arid Environ. https://doi.org/10.1016/j.jaridenv.2017.11.002.

Thompson, G., M. Tewari, K. Ikeda, S. Tessendorf, C. Weeks, J. A. Otkin, and F. Kong, 2016: Explicitly-coupled cloud physics and radiation parameterizations and subsequent evaluation in WRF high-resolution convective forecasts. Atmos. Res., 168, 92–104, https://doi.org/10.1016/j.atmosres.2015.09.005.

Tubi, A., and U. Dayan, 2014: Tropical plumes over the Middle East: Climatology and synoptic conditions. Atmos. Res., 145–146, 168–181, https://doi.org/10.1016/j.atmosres.2014.03.028.

Viswanadhapalli Y., H. P. Dasari, S. Langodan, V. S. Challa, and I. Hoteit, 2016: Climatic features of the Red Sea from a regional assimilative model. Int. J. Climatol., 37, 2563-2581, http://dx.doi.org/10.1002/joc.4865.

Wang Y., L. R. Leung, J. L. McGregor, D. K. Lee, W. C. Wang, Y. Ding, and F. Kimura, 2004: Regional climate modeling: progress, challenges and prospects. J. Meteor. Soc. Jpn., 82(6),1599–1628, https://doi.org/10.2151/jmsj.82.1599.

Wang, Q., M. Xue, and Z. Tan, 2016: Convective initiation by topographically induced convergence forcing over the Dabie Mountains on 24 June 2010. Advances in Atmospheric Sciences, 33(10), 1120– 1136, https://doi.org/10.1007/s00376-016-6024-z.

Wilks, D., 2006: Statistical Methods in the Atmospheric Sciences: An Introduction. 2nd ed. Academic Press, 627 pp.

Accepted for publication in *Journal of Hydrometeorology*. DOI 10.1175/JHM-D-19-0114.1.

Yadav, R.K., D. A. Ramu, and A. P. Dimri, 2013: On the relationship between ENSO patterns and winter precipitation over North and Central India. Global Planet. Change, 107, 50–58. doi:10.1016/j.gloplacha.2013.04.006.

Yanai, M., S. Esbensen, and J. Chu, 1973: Determination of the bulk properties of tropical cloud clusters from large heat and moisture budgets. J. Atmos. Sci., 30, 611–627.

Yuan, X., X. Z. Liang, and E. Wood, 2012: WRF ensemble downscaling seasonal forecasts of China winter precipitation during 1982–2008. Climate Dyn., 39, 2014–2058, doi: 10.1007/s00382-011-1241-8.

Zittis, G., and P. Hadjinicolaou, 2017: The effect of radiation parameterization schemes on surface temperature in regional climate simulations over the MENA-CORDEX domain. Int. J. Climatol., 37, 3847–3862, https://doi.org/10.1002/joc.4959.

Zittis, G., P. Hadjinicolaou, and J. Lelieveld, 2014: Comparison of WRF model physics parameterizations over the MENA-CORDEX domain. Am. J. Clim. Change, 3, 490–511, doi: 10.4236/ajcc.2014.35042.

Ziv, B., 2001: A subtropical rainstorm associated with a tropical plume over Africa and the Middle-East. Theor. Appl. Climatol. 69, 91–102, https://doi.org/10.1007/s007040170037.

Zolina, O., A. Dufour, S. Gulev, and G. Stenchikov, 2017: Regional hydrological cycle over the Red Sea in ERA-Interim. J. Hydrometeor., 18, 65–83, https://doi.org/10.1175/JHM-D-16-0048.1.

Accepted for publication in *Journal of Hydrometeorology*. DOI 10.1175/JHM-D-19-0114.1.

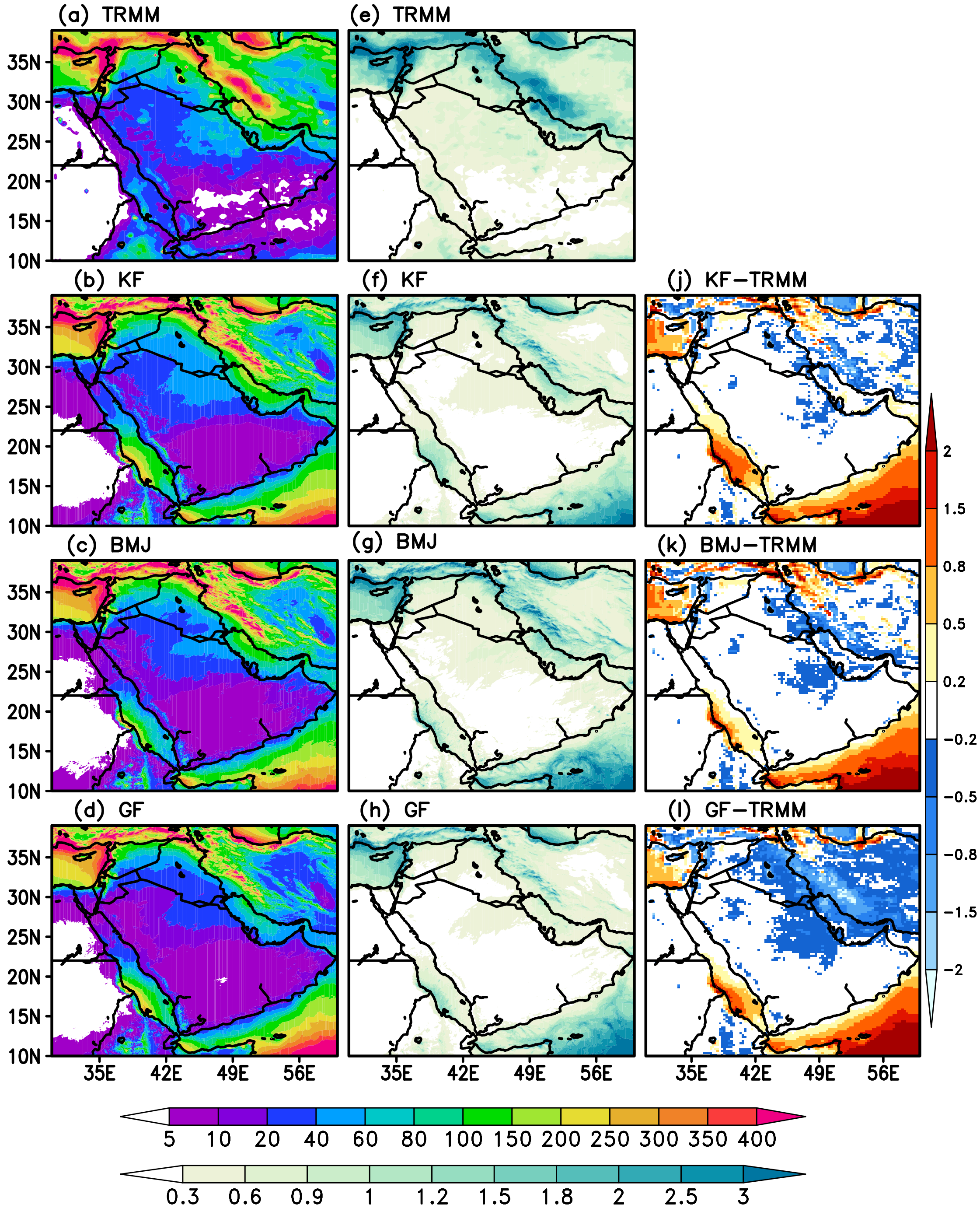

Figure 1. Spatial distribution of mean total winter rainfall (mm; a-d) and its standard deviation (mm day^{-1}; e-h) from TRMM, KF, BMJ and GF schemes. Mean rainfall biases (i-l) between model simulations and observations (significant at 95% confidence level).

Accepted for publication in *Journal of Hydrometeorology*. DOI 10.1175/JHM-D-19-0114.1.

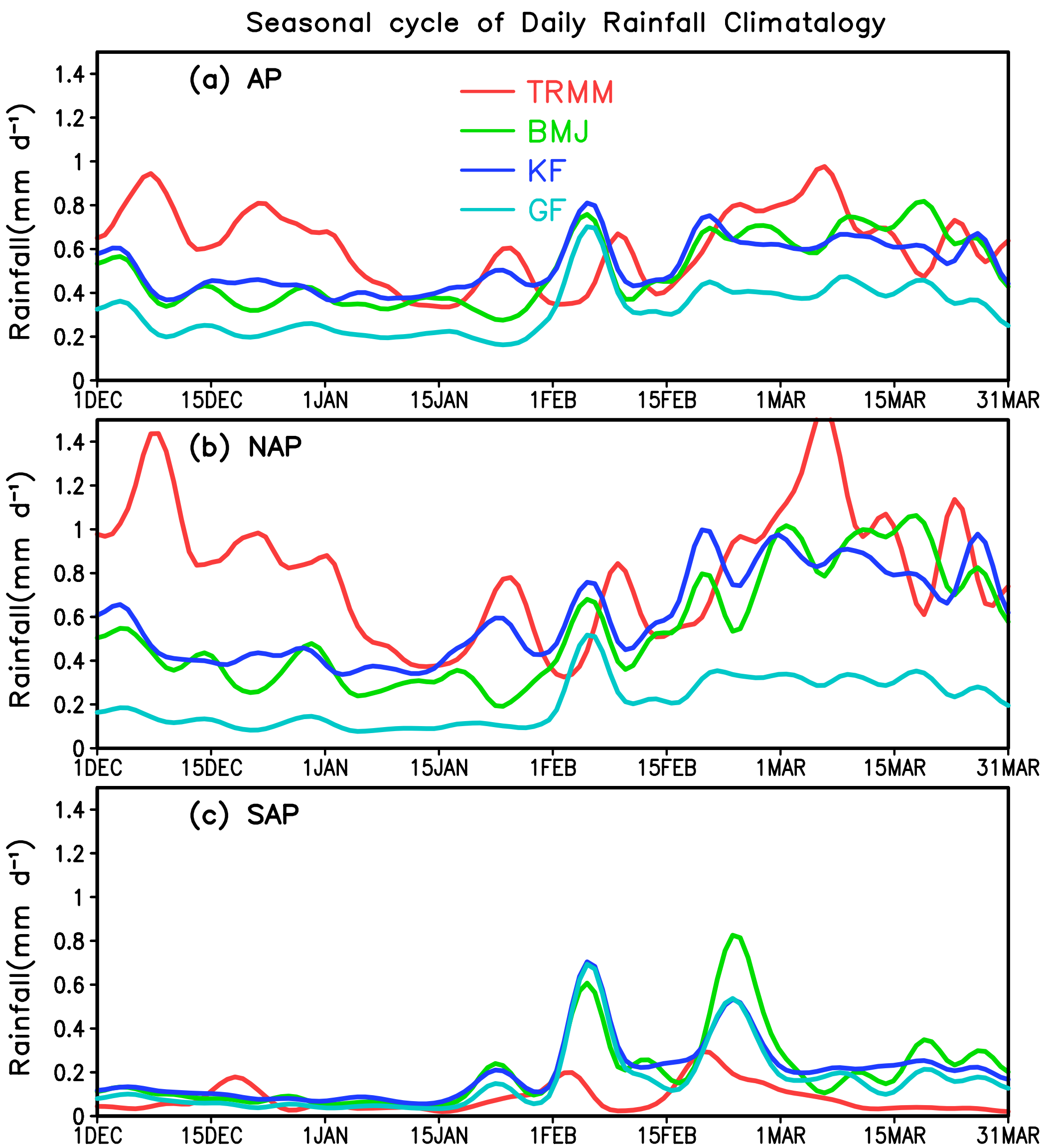

Figure 2. Seasonal cycle of daily rainfall climatology over (a) AP, (b) NAP and (c) SAP sub-regions from TRMM, KF, BMJ and GF cumulus parameterization schemes.

Accepted for publication in *Journal of Hydrometeorology*. DOI 10.1175/JHM-D-19-0114.1.

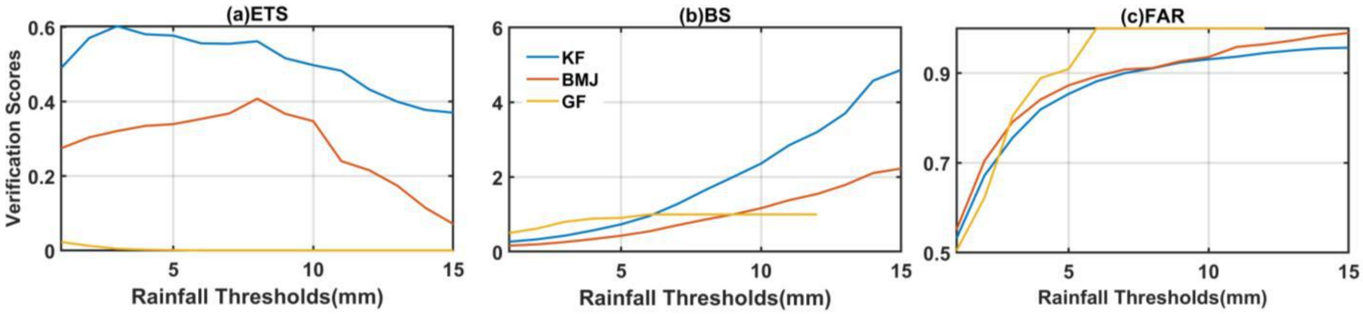

Figure 3. Verification skill scores for the simulated rainfall from KF, BMJ and GF at different rainfall thresholds over the NAP.

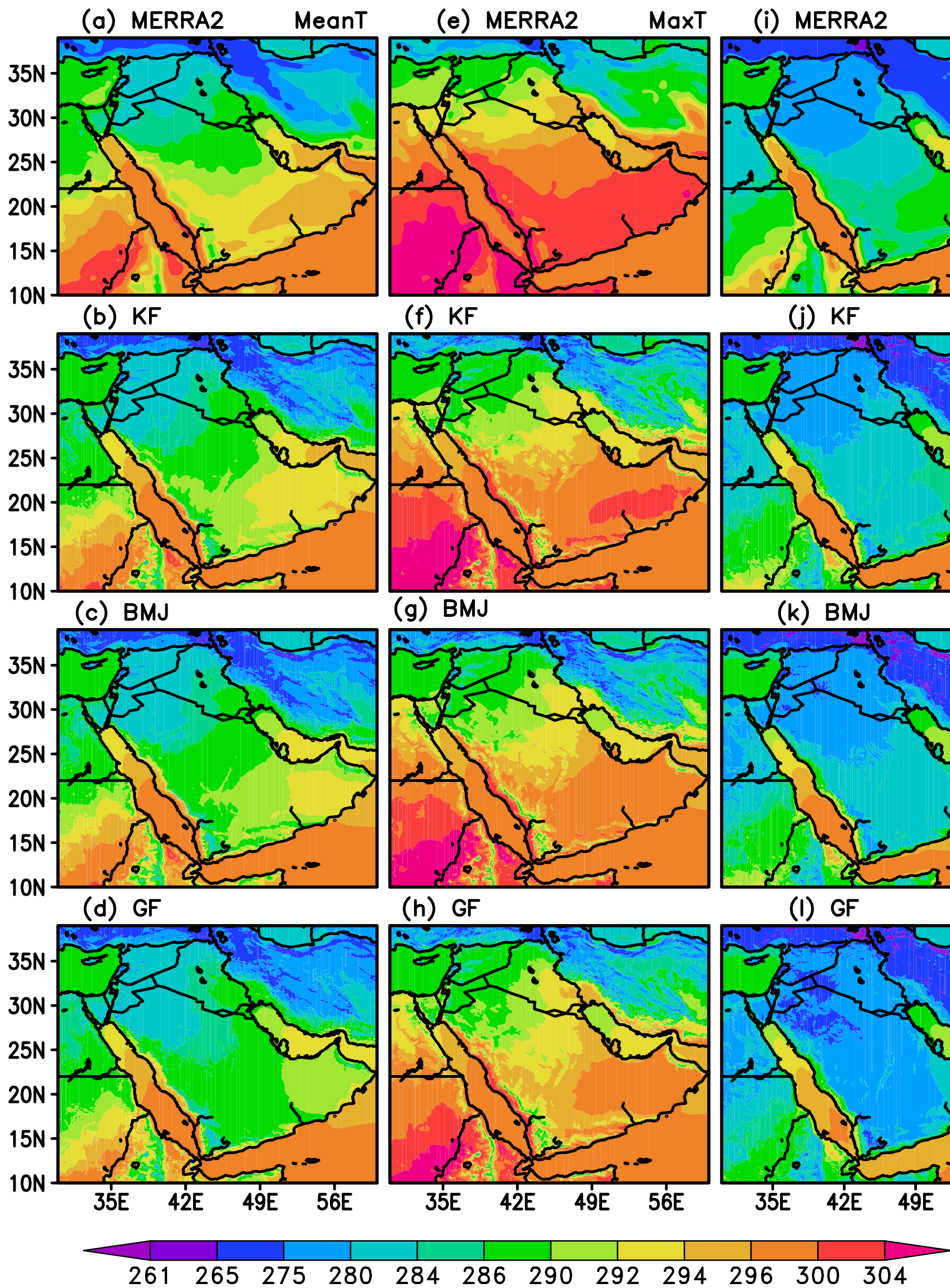

Figure 4. Spatial distribution of winter season mean surface temperature (K; a-b), maximum temperature (K; e-h) and minimum temperature (K, i-l) averaged over the period 2001-2016 from MERRA2, KF, BMJ and GF.

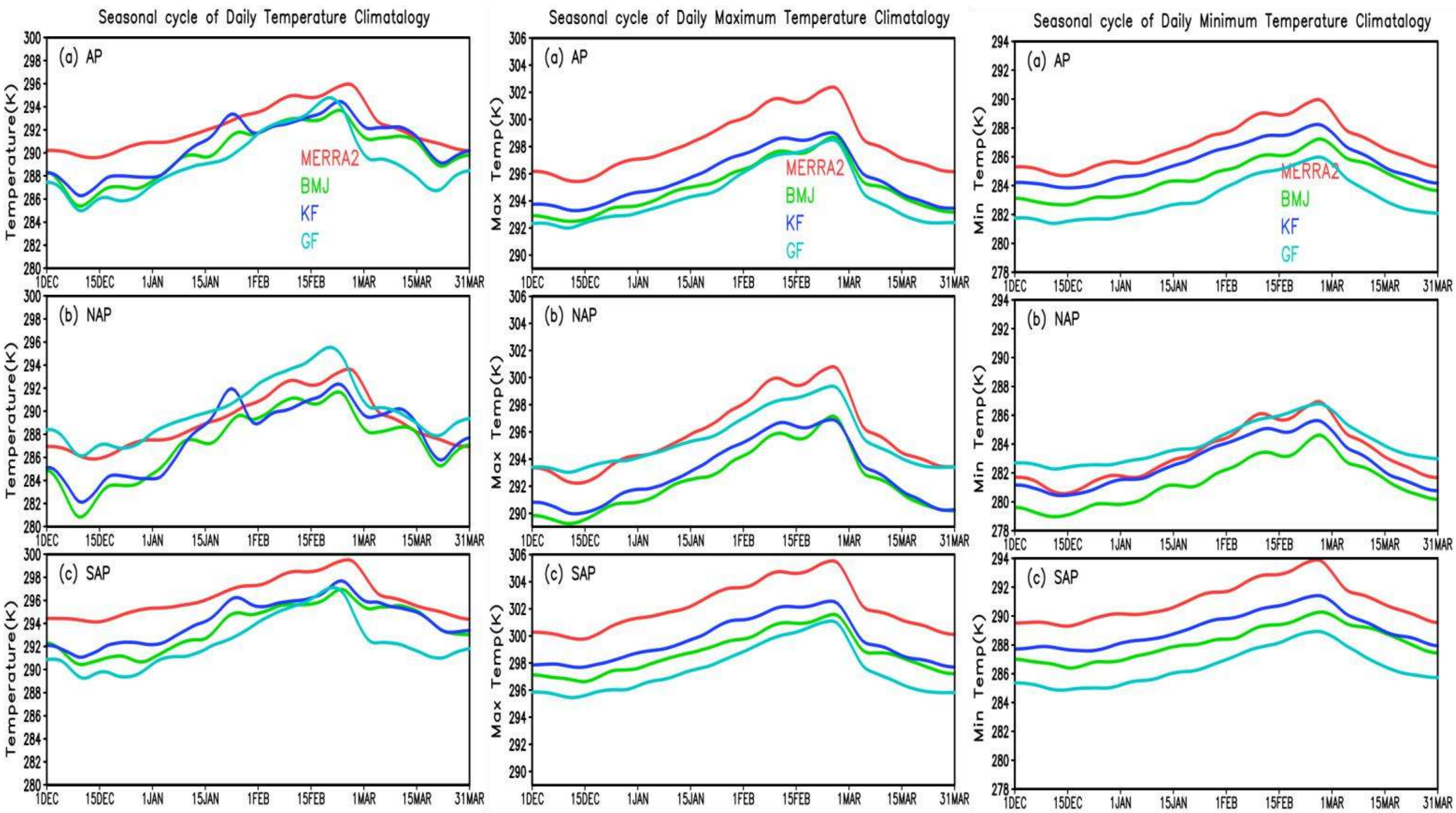

Figure 5. Seasonal cycle of daily mean surface temperature (K), maximum temperature (K) and minimum temperature climatology over (a) AP, (b) NAP and (c) SAP sub-regions from MERRA2, KF, BMJ and GF cumulus parameterization schemes averaged over the period 2001-2016.

Accepted for publication in *Journal of Hydrometeorology*. DOI 10.1175/JHM-D-19-0114.1.

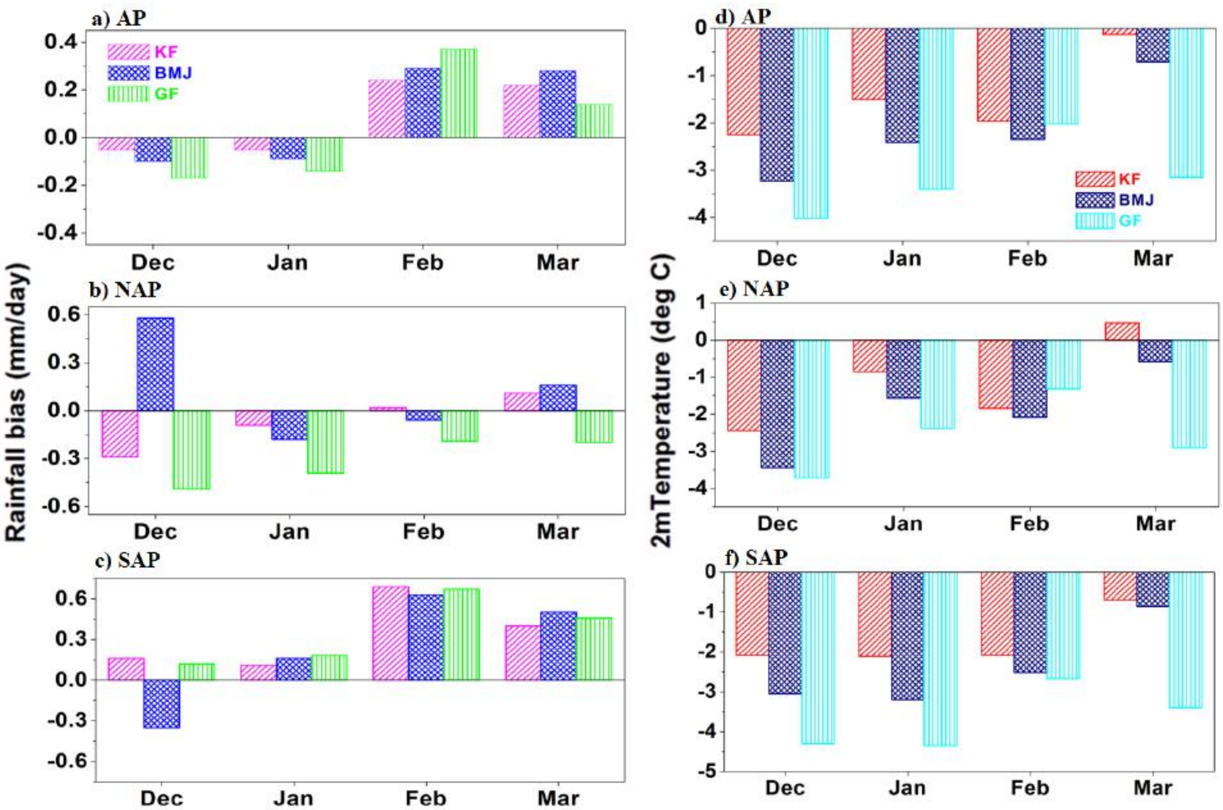

Figure 6. Sub-regional average bias of rainfall (a-c) and 2 meter air temperature (d-f) from KF, BMJ and GF over the (a) AP, (b) NAP and (c) SAP during winter.

Accepted for publication in *Journal of Hydrometeorology*. DOI 10.1175/JHM-D-19-0114.1.

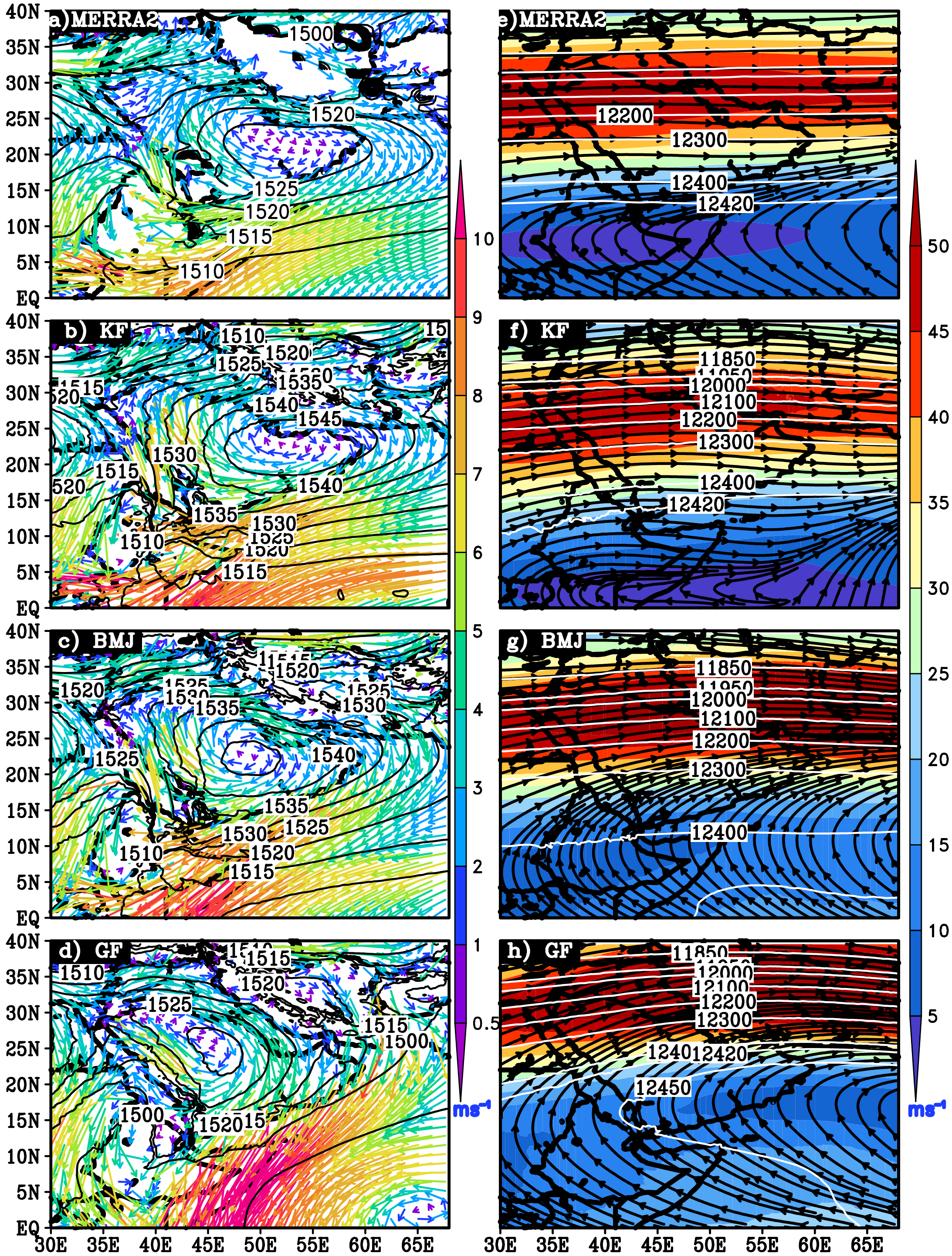

Figure 7: Winter seasonal mean (left panel) low level (850 hPa) and upper level (right panel) wind speed (shaded; ms^{-1}), direction (vectors) and geopotential height (m) from MERRA2 (a,e), KF(b,f), BMJ (c,g) and GF (d,h) averaged over 2001-2016.

Accepted for publication in *Journal of Hydrometeorology*. DOI 10.1175/JHM-D-19-0114.1.

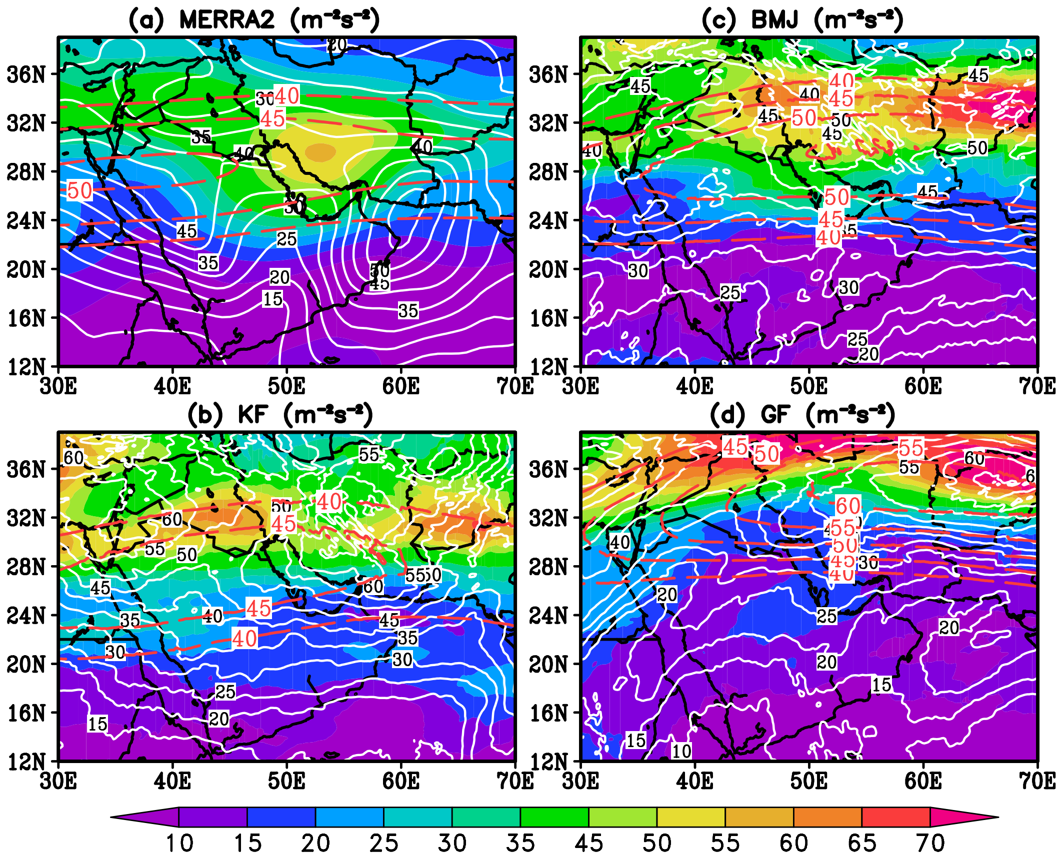

Figure 8: Spatial distribution of winter mean upper tropospheric (200 hPa) synoptic transients in the zonal (shaded) and meridional wind components (contours) from MERRA2 and three different cumulus parameterization schemes. Red contour indicate the wind maxima (above 40 ms^{-1}) of upper level (200 hPa) zonal winds (ms^{-1}).

Accepted for publication in *Journal of Hydrometeorology*. DOI 10.1175/JHM-D-19-0114.1.

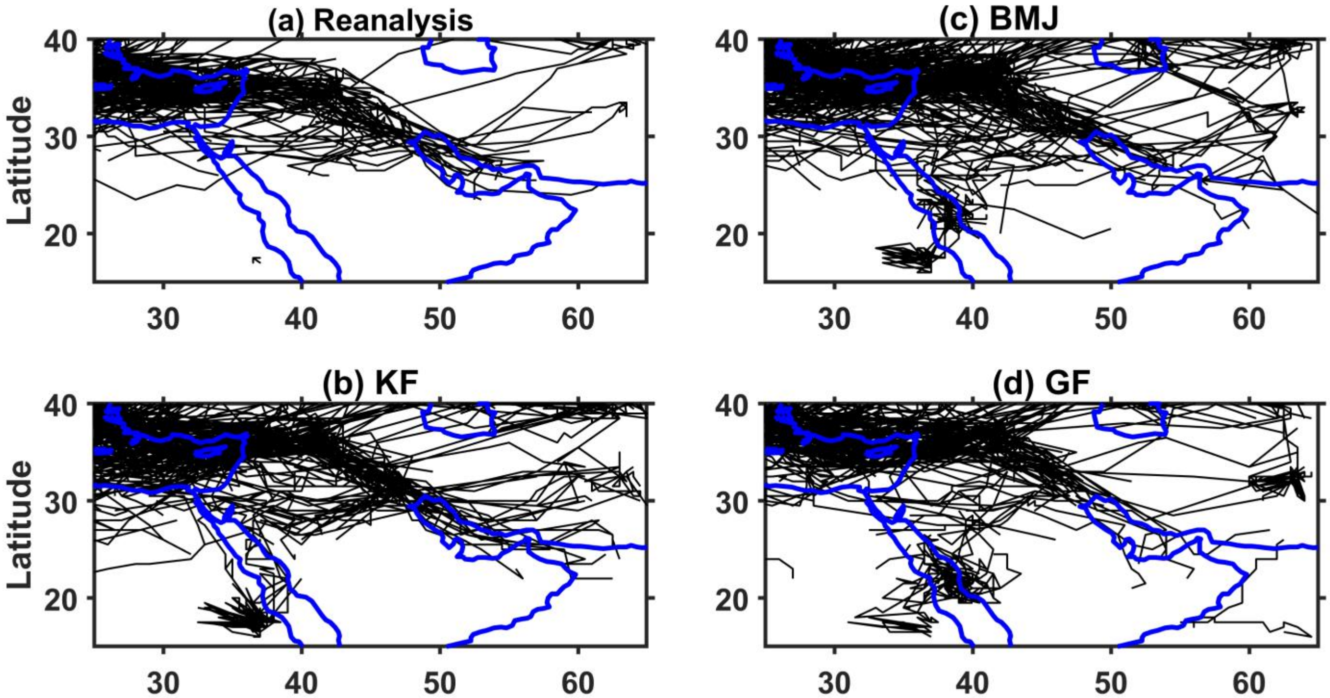

Figure 9: Storm tracks associated with AP winter rainfall for the period 2001-2016 from (a) reanalysis, (b) KF, (c) BMJ and (d) GF. Here we present the tracks cover the whole lifetime of the storms from their formation to dissipation.

Accepted for publication in *Journal of Hydrometeorology*. DOI 10.1175/JHM-D-19-0114.1.

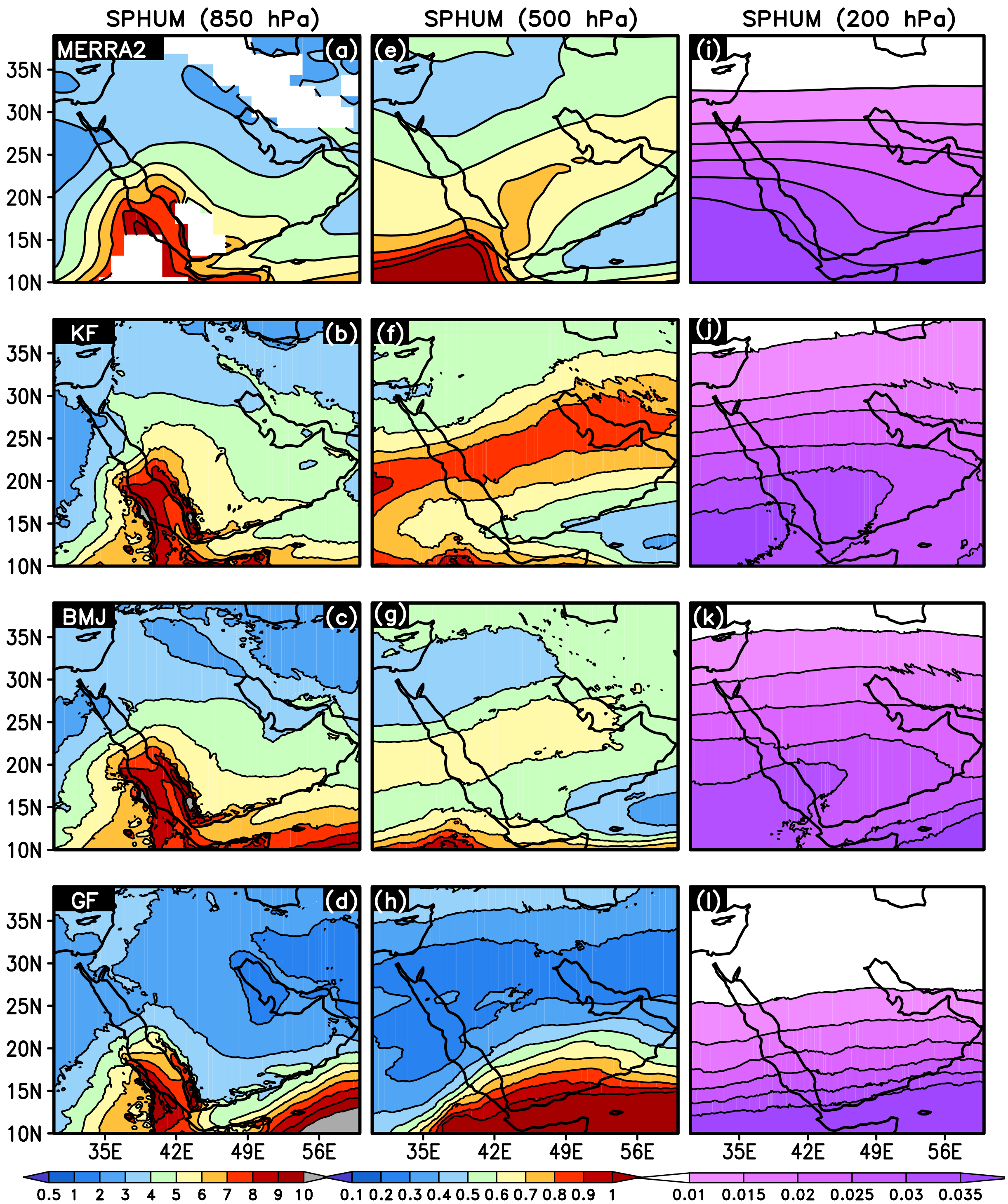

Figure 10: Spatial distribution of seasonal mean low level (850 hPa), middle level (500 hPa) and upper level (200 hPa) specific humidity (contours; g.kg^{-1}) during winter from MERRA2, KF, BMJ and GF.

Accepted for publication in *Journal of Hydrometeorology*. DOI 10.1175/JHM-D-19-0114.1.

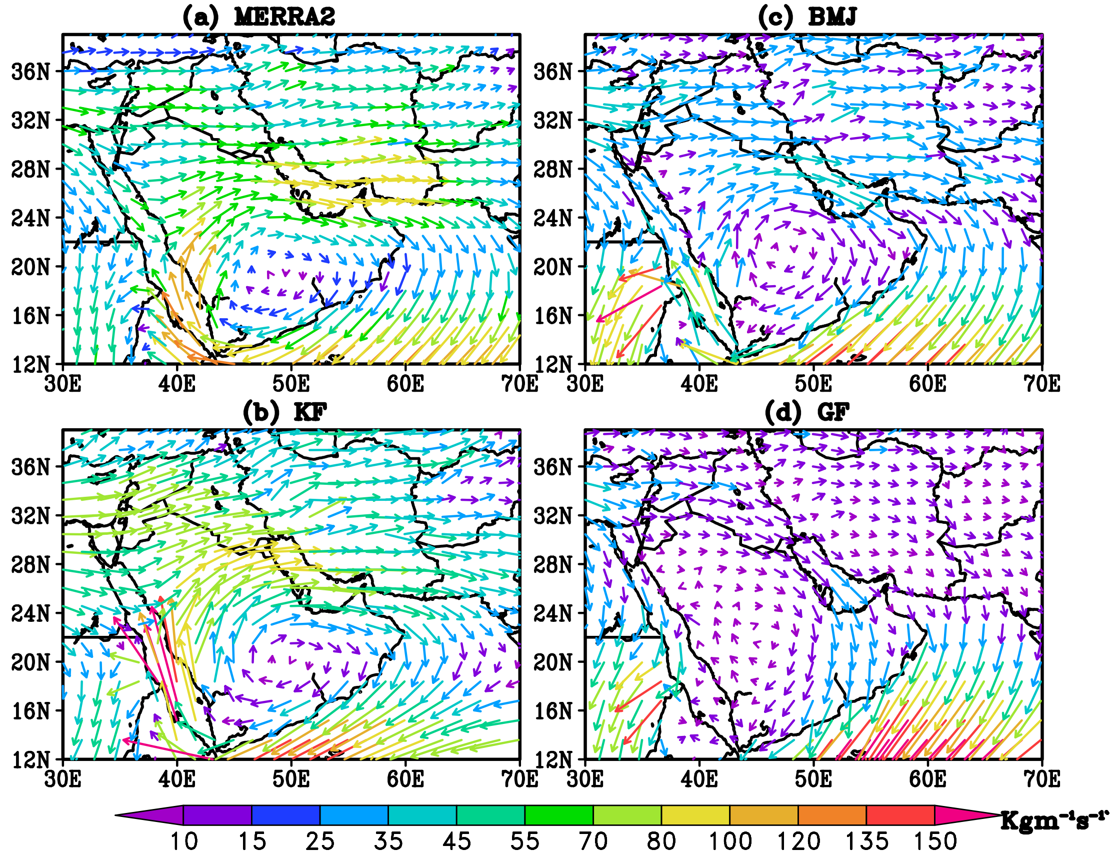

Figure 11: Vertically integrated moisture transport during winter season from MERRA2, KF, BMJ and GF for the period 2001-2016.

Accepted for publication in *Journal of Hydrometeorology*. DOI 10.1175/JHM-D-19-0114.1.

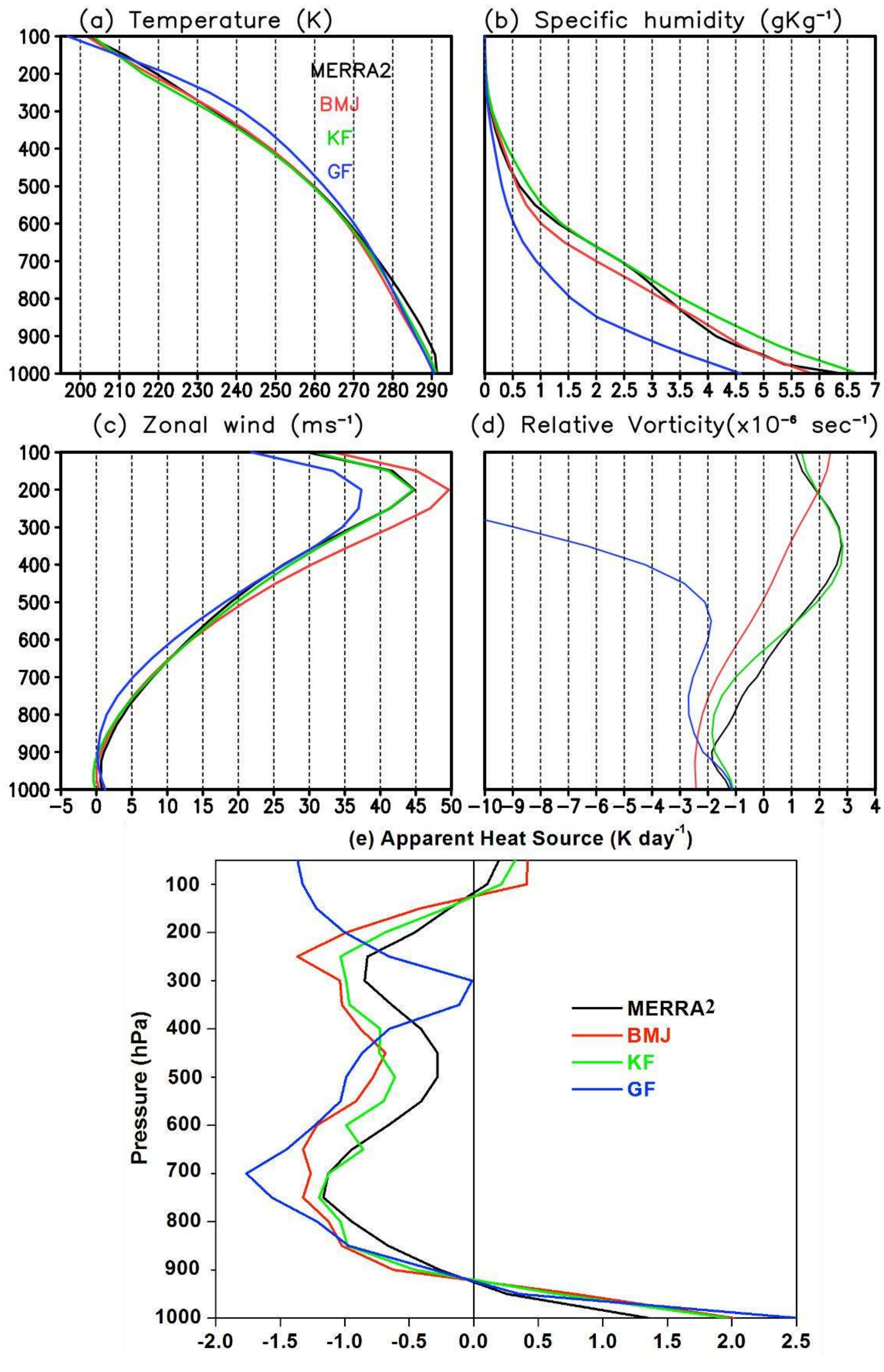

Figure 12. Area averaged winter mean vertical profiles of (a) temperature, (b) specific humidity, (c) zonal wind (d) relative vorticity and (e) apparent heat source over the NAP sub-region from MERRA2 and model simulations for the period 2001-2016.

Accepted for publication in *Journal of Hydrometeorology*. DOI 10.1175/JHM-D-19-0114.1.

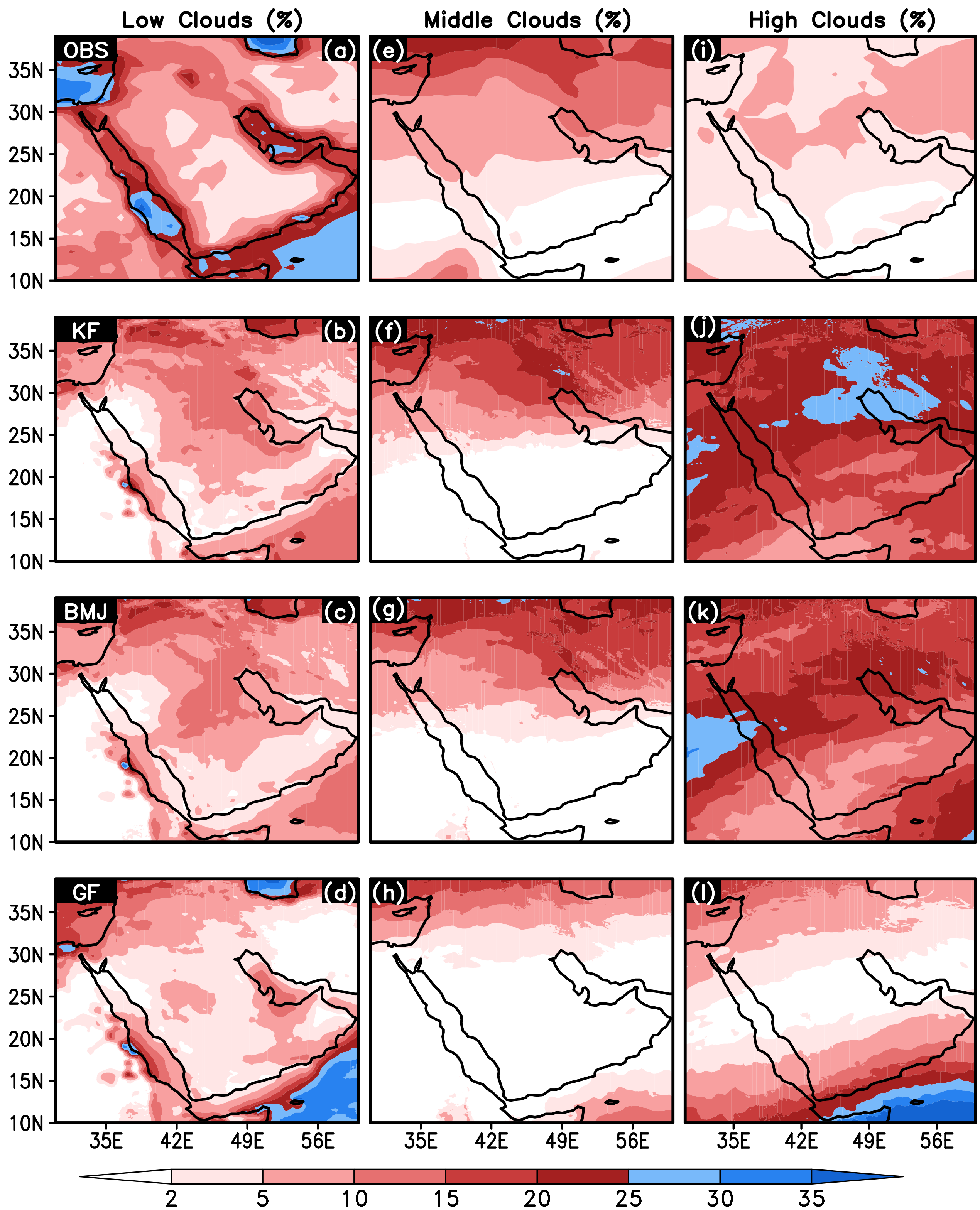

Figure 13. Spatial distribution of seasonal mean low level cloud cover (a-d), middle level cloud cover (e-h) and high level cloud cover (i-l) during winter from observations and model simulations for the period 2001-2016.

Accepted for publication in *Journal of Hydrometeorology*. DOI 10.1175/JHM-D-19-0114.1.

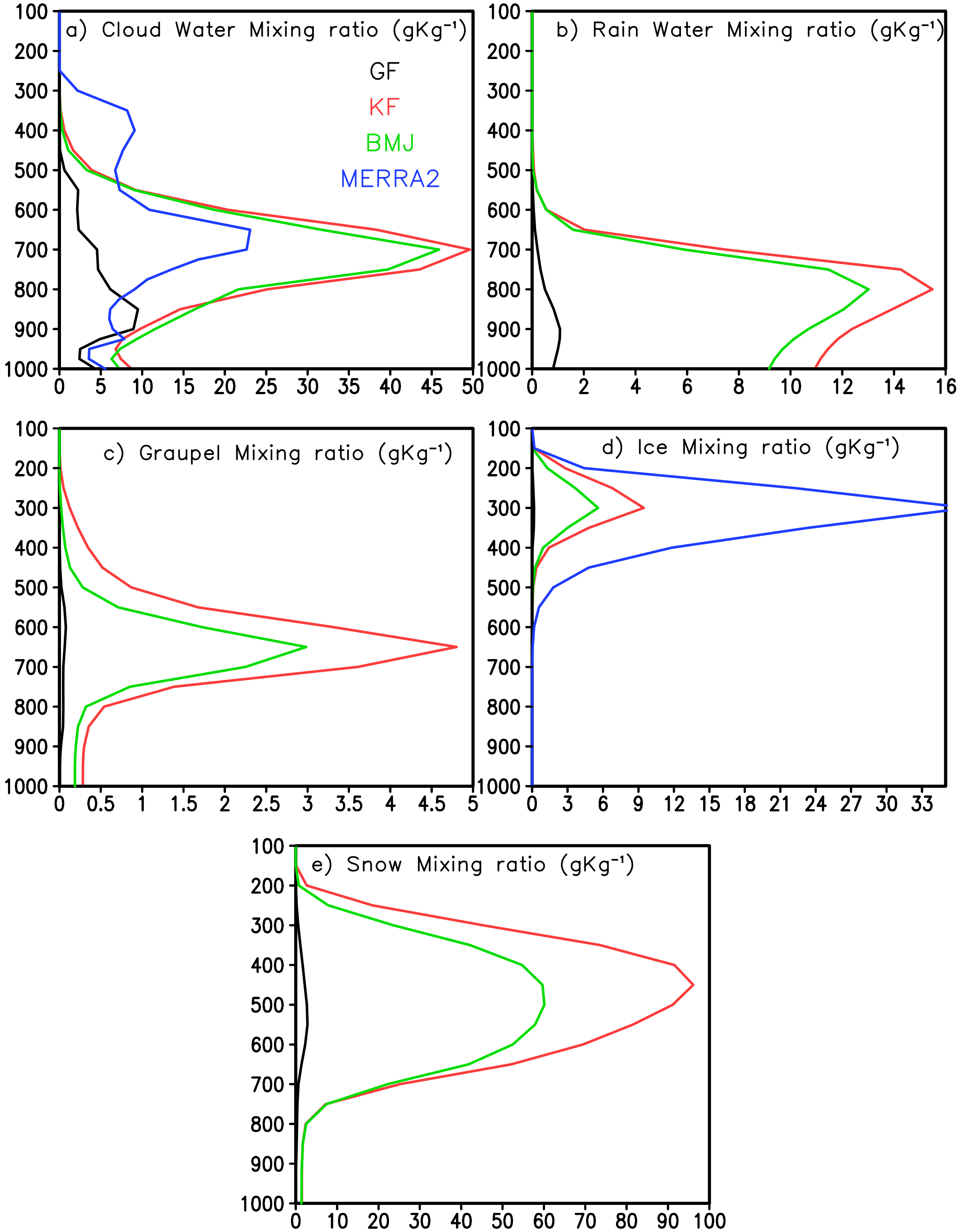

Figure 14. Spatial and temporal means of vertical profiles of cloud hydrometeors provided by the different schemes, corresponding to the winter season and computed for northern AP region: (a) cloud water, (b) rainwater, (c) graupel, (d) ice, (e) snow.

Accepted for publication in *Journal of Hydrometeorology*. DOI 10.1175/JHM-D-19-0114.1.

Expts.	Std. Div (mmd^{-1})				Mean bias (mmd^{-1})				RMSE (mmd^{-1})				Pattern CC			
	AP	NAP	SAP	NEAP	AP	NAP	SAP	NEAP	AP	NAP	SAP	NEAP	AP	NAP	SAP	NEAP
OBS	0.57	0.85	0.30	1.10												
KF	0.60	0.47	0.49	1.03	0.15	-0.07	0.37	-0.14	0.29	0.16	0.42	0.22	0.71	0.88	0.22	0.90
BMJ	0.61	0.58	0.63	0.77	0.19	-0.14	0.31	-0.17	0.31	0.18	0.37	0.38	0.66	0.85	0.16	0.89
GF	0.44	0.35	0.53	0.60	-0.30	-0.45	0.34	-0.43	0.37	0.41	0.40	0.55	0.19	0.66	0.23	0.61

Table 1. Statistical skill scores for mean daily rainfall (mm d^{-1}) during the winter season (DJFM) over the AP and its different sub-regions for the period 2001–2016 from model simulations with different convection schemes and observations.

Accepted for publication in *Journal of Hydrometeorology*. DOI 10.1175/JHM-D-19-0114.1.

Mean Temperature

Expts.	Std. Div (K)				Mean bias (K)				RMSE (K)				Pattern CC			
	AP	NAP	SAP	NEAP	AP	NAP	SAP	NEAP	AP	NAP	SAP	NEAP	AP	NAP	SAP	NEAP
OBS	2.12	2.59	1.68	2.74												
KF	2.97	3.76	2.23	3.73	-1.4	-1.18	-1.7	-0.87	2.06	2.25	1.89	1.64	0.96	0.96	0.92	0.97
BMJ	3.07	3.73	2.45	3.84	-2.1	-1.9	-2.43	-1.7	1.9	1.96	1.93	1.86	0.96	0.95	0.93	0.96
GF	3.30	4.04	2.62	4.14	-3.1	-2.5	-3.6	-2.07	3.3	2.9	3.6	2.4	0.93	0.93	0.91	0.95
Maximum Temperature																
OBS	2.3	2.9	1.8	3.0												
KF	2.1	2.5	1.7	2.6	-2.8	-3.0	-2.6	-3.2	2.9	3.1	2.6	3.6	0.91	0.91	0.75	0.94
BMJ	2.0	2.5	1.6	2.7	-3.5	-3.6	-3.4	-3.8	3.4	3.6	3.2	4.0	0.89	0.89	0.67	0.94
GF	2.2	2.7	1.8	2.8	-4.1	-3.6	-4.5	-3.4	4.1	3.7	4.5	3.6	0.84	0.86	0.54	0.92
Minimum Temperature																
OBS	1.7	2.1	1.4	2.2												
KF	1.5	1.8	1.2	1.9	-1.2	-0.6	-1.9	-0.5	1.4	1.2	1.6	1.5	0.97	0.97	0.97	0.97
BMJ	1.5	1.7	1.2	1.9	-2.4	-1.9	-2.8	-1.8	2.2	2.0	2.5	2.1	0.97	0.93	0.97	0.95
GF	1.6	1.8	1.3	1.9	-4.0	-3.5	-4.4	-3.2	3.8	3.5	4.1	3.3	0.96	0.95	0.97	0.6

Table 2. Statistical skill scores for mean daily 2m mean, maximum and minimum temperatures (K) during the winter season (DJFM) over the AP and its different sub-regions for the period 2001–2016 from model simulations with different convection schemes and observations.

Accepted for publication in *Journal of Hydrometeorology*. DOI 10.1175/JHM-D-19-0114.1.